Use this document as a template

My PhD Thesis

Customise this page according to your needs

Tobias Hangleiter*

June 13, 2025

^{*} A LaTeX lover/hater



Contents

Co	Contents		
Ι	A FLEXIBLE PYTHON TOOL FOR FOURIER-TRANSFORM NOISE SPECTROSCOPY		
II	I CHARACTERIZATION AND IMPROVEMENTS OF A MILLIKELVIN CONFOCAL MICROSCOPE		
1	Introduction	3	
2	Characterization of the cryostat performance 2.1 Cooling power	4 4 6	
3	Optical path 3.1 Light coupling	10 10 10 14 16 18	
4	Vibration noise 4.1 Vibration isolation	20 21 21 22 23 24 27 29	
5	Conclusion & outlook	31	
	OPTICAL MEASUREMENTS OF ELECTROSTATIC EXCITON TRAPS IN SEMICON- DUCTOR MEMBRANES A FILTER-FUNCTION FORMALISM FOR UNITAL QUANTUM OPERATIONS	32	
1 4	TITLETER TONCTION TORMALISM TOR ONITAL QUANTUM OF ERATIONS	33	
Aı	PPENDIX	34	
A	Optical coupling A.1 Collection efficiency	35 35 36 37	
В	Vibration spectroscopy B.1 Knife-edge measurement	39 39	

List of Terms 40

List of Figures

2.1	Generated by img/py/setup/cooling_power.py
2.2	Generated by img/py/setup/cooling_power.py
2.3	Generated by img/py/setup/cooling_power.py
2.4	Generated by img/py/setup/transport.py
2.5	Generated by img/py/setup/transport.py 8
2.6	Generated by img/py/setup/transport.py
3.1	Generated by img/tikz/setup/optical_path.tex
3.2	Generated by img/py/setup/single_mode_fiber_coupling.py
3.3	Generated by img/tikz/setup/emission.tex
3.4	Generated by img/py/setup/extraction.py
3.5	Generated by img/py/setup/extraction.py
3.6	Generated by img/py/setup/imaging.py
3.7	Generated by img/py/setup/g2.py 18
3.8	Generated by img/py/setup/g2.py
4.1	Generated by img/pdf/setup/springs.py
4.2	Generated by img/py/setup/vibration_spectroscopy.py
4.3	Generated by img/tikz/setup/knife_edge.tex
4.4	Generated by img/py/setup/vibration_spectroscopy.py
4.5	Generated by img/py/setup/vibration_spectroscopy.py
4.6	Generated by img/py/setup/vibration_spectroscopy.py
4.7	Generated by img/py/setup/vibration_spectroscopy.py
4.8	Generated by img/pdf/setup/vibration_spectroscopy.py
5.1	Generated by img/py/setup/vibration_spectroscopy.py
B.1	

Publications

Software

The following open-source software packages were developed (at least partially) during the work on this thesis.

Part I

A FLEXIBLE PYTHON TOOL FOR FOURIER-TRANSFORM NOISE SPECTROSCOPY

Part II

CHARACTERIZATION AND IMPROVEMENTS OF A MILLIKELVIN CONFOCAL MICROSCOPE

Introduction 1

bottom loading
2. recap optical setup, both on the fridge and optical table
3. setup automation

Characterization of the cryostat performance

N essential feature of the confocal microscope discussed in the present thesis is its capability to perform optical measurements at Millikelvin temperatures. As individual quantum systems are singled out for applications in quantum technology, thermal excitations with energy $k_{\rm B}T=86\,\mu{\rm eV/K}\times T$ quickly become the dominating energy scale and overshadow the desired effects. Hence, typical energies in the solid state on the $\mu{\rm eV}$ scale, such as Zeeman energies of individual spins with energy $\mu_{\rm B}B=58\,\mu{\rm eV/T}\times B$, require temperatures well below 1 K to suppress thermal excitations.

By design the Oxford Instruments Triton 450 dry dilution refrigerator (DR) housing the microscope is rated for base temperatures at the mixing chamber plate below $T_{\rm MXC}=10\,{\rm mK}$. However, several factors, both passive and active, introduce additional heat loads that can potentially raise the base temperature if too large:

- 1. DC and RF wiring. These introduce thermal links between the sample and higher temperature stages as well as add noise that raises the electron temperature in the sample.
- Wiring and operation of the Attocube ANPx311 nanopositioners.
 The nanopositioners require special low-impedance connections to ensure a large enough bandwidth for the stick-slip mode of operation. Moreover, the resistive position readout introduces additional heating.
- 3. Optical access. The free-space optical access requires a direct line-of-sight (LOS) port to the sample. This inevitably allows infrared radiation from room temperature into the cryostat, something that is usually painstakingly prevented when designing a cryostat. Furthermore, optical experiments involve irradiating the sample with a highly focused laser beam, some of which will be absorbed and contribute to heating.

In this chapter, I characterize the cooling performance of the dry DR housing the microscope in various ways. I first discuss the cooling power in terms of the base temperature $T_{\rm MXC}$ reached for different configurations in Section 2.1. This is often quoted as the bath, lattice, or *phonon* temperature, and can be read out using the resistive RuO₂ thermometry setup installed in the DR. Then, in Section 2.2, I present measurements of the *electron* temperature, a quantity that is arguably more expressive of the cryostat's capability to perform precise measurements as it is more sensitive to, for example, electrical noise introduced by the wiring.

2.1 Cooling power

The base temperature ($T_{\rm MXC}$) can be read out from the resistance bridge connected to the gas handling PC controlling the cryostat. Two different thermometers are installed on the mixing chamber, a Cernox® sensor that works in the range from room temperature down to around 2 K for cooldown, and a RuO₂ sensor that works from 30 K down to, in principle, zero for base temperature operation. The resistance bridge performs a four-terminal measurement of the sensor resistance and converts it to a temperature according to a sensor-specific calibration $T_{\rm MXC}(R_{\rm RuO_2})$.

1: This terminology can be misleading as the phonon temperature can also be measured with a quantum transport device, which will most likely see a different phonon temperature than the thermometer on the mixing chamber plate because of a temperature gradient between the heating source close to the sample and sink (the mixing chamber) close to the thermometer.

Since the particular sensor installed in our system was only calibrated down to 30 mK, I had to extrapolate the calibration curve as the system reaches lower temperatures than this, and hence the temperatures below this threshold quoted here are not guaranteed to be correct.

With the configuration described in Reference **Descamps2021**, the DR reached a base temperature of $T_{\rm MXC}=30\,{\rm mK}$. This included all DC and RF wiring as well as a single anti-reflection (AR)-coated window sealing the vacuum space on top of the fridge for optical access. To investigate the influence of ambient thermal radiation entering the cryostat through the optical access port, or, more generally, radiation from the higher-to lower-temperature stages, I measured the base temperature for two additional configurations; once with an additional AR-coated window inserted into the optical path on the Cold plate, and once with three windows installed on the first pulse tube stage (PT1), second pulse tube stage (PT2), and Still plates. The windows (Thorlabs WW41050-B) are made from UV fused silica with AR coating The manufacturer quotes a typical reflectance of 0.25 % in the relevant wavelength range, while the glass is largely transmissive for wavelengths below $\lambda_{\rm cutoff}\sim 4.5\,{\rm \mu m}$. Since the spectral radiance of thermal black-body radiation [**Planck1900**]

$$B_{\lambda}(\lambda, T) = \frac{2hc^2}{\lambda^5} \frac{1}{\exp(hc/\lambda k_{\rm B}T) - 1}$$
 (2.1)

is small up to $\lambda_{\mathrm{cutoff}}$ at low (\leq 300 K) temperatures as shown in Figure 2.1, we expect the windows be largely opaque to thermal radiation and hence be quite effective in reducing the radiative heat load. As the radiative power scales with T^4 and there is at the same time more cooling power available at higher-temperature stages, installing windows there result in an overall better performance.

Table 2.1 shows the measured mixing chamber temperatures for the different window configurations. Indeed, already a single window installed on the Cold plate significantly reduces the base temperature. While the windows do introduce additional reflections of the laser spot when imaging the sample due to the finite remaining reflectance, their intensity is low enough, and their position on the camera far enough away from the main spot to be an issue. On the contrary, their presence can be quite useful when aligning the laser spots from the two arms of the optical head by aligning them in such a way that the reflections overlap.

Besides the ambient radiation, there is also the heat load introduced by the partial absorption of the laser excitation during optical measurements. In order to characterize both the heat load and measure the absorptance A of our sample, I irradiated a flip-chip-bonded membrane sample such as measured in Part III with the laser at 815 nm and measured the increase in base temperature. The sample consists of a 220 nm thick GaAs/AlGaAs membrane glued with epoxy to a Si host substrate chip for handling. As the samples are flip-chip bonded, light that is transmitted through the chip without being absorbed or reflected will then hit the surrounding puck and scatter. Thus, to be precise, I measured A+T this way, where T is the transmittance, assuming that light that exits the membrane will be absorbed somewhere and contribute to heating. I will nonetheless refer to the measured quantity as simply A.

With the power meter mounted in the transmission direction of the excitation arm of the optical head (*cf.* Figure 3.1), I measured the amount of power directed towards the sample by scaling the measured power with the ratio of transmittance and reflectance of the beam splitter (BS),

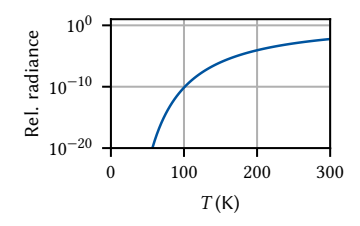


Figure 2.1: Relative black-body radiance obtained by integrating Equation 2.1 from $\lambda = 0 \, \mu \text{m}$ to 4.5 μm and normalizing to the total radiance. At $T = 300 \, \text{K}$, the fraction of total radiance residing in the high-energy part of the spectrum is still only 0.6 %.

2: Depending on the manufacturer, the coating for the range 650 nm to 1050 nm is called BBAR VIS-NIR or BBAR-B.

Table 2.1: Mixing chamber (MXC) temperature for different configurations of AR coated windows (Thorlabs WW41050-B) inside the DR.

Windows	$T_{ m MXC}$ (MK)
None	30.0
Cold	11.0
PT1, PT2, Still	7.9

I / we, general rephrasing

 $T \div R \approx 15$. Assuming negligible losses on the way towards the sample, I then recorded the mixing chamber temperature as function of laser power. To relate that change in temperature to a heat load \dot{Q} deposited on the sample, I calibrated the cooling power of the DR using the builtin heaters. Setting a heater power and waiting for the mixing chamber temperature to settle thus yields the cooling power $P_{\rm cool}$ as function of temperature $T_{\rm MXC}$, which is expected to follow the quadratic relationship [**DeWaele2011**]

$$P_{\text{cool}} = \dot{Q} = \alpha T_{\text{MXC}}^2 + \beta. \tag{2.2}$$

As a last step, we can use a simple model of absorption of the laser on the sample in thermal equilibrium,

$$P_{\text{cool}} = P_{\text{nr}} = AP_{\text{laser}},$$
 (2.3)

where $P_{\rm nr}$ is the amount of power deposited into nonradiative emission channels causing heating of the lattice, to relate the incident laser power $P_{\rm laser}$ to the cooling power and thus obtain the absorptance A.

Figure 2.2 shows data sets obtained with the MXC heater (magenta) and laser (green). The solid lines are fits to Equation 2.2 including the solid data points only as at low powers there is clearly a deviation from the square-root relationship between the two. Comparing the fit results for α , we obtain A=28.5%. Alternatively, we can fit a quadratic smoothing spline to the laser data (magenta dashed line) and fit a version scaled according to Equation 2.3 to the heater data (green dashed line). This yields A=28.1% in good agreement to the value obtained from fitting the theoretical model. Furthermore, the data shows that only at laser powers above 10 μ W the MXC heats up appreciably.

Lastly, let us address the impact of the Attocube ANPx311 position readout. The nanopositioners are crucial in the operation of the microscope as they are used to position the sample with respect to the focal spot of the objective lens. They operate in slip-stick mode which naturally generates heat through friction when moving. However, the resistive position readout also contributes to heating, so in order to assess if the readout should be switched off when it is not required to avoid unnecessarily elevated cryostat temperatures, I measured $T_{\rm MXC}$ as a function of readout voltage. Note that the Attocube ANC350 piezo controller offers the option of lock-in measurement for readout, which should be enabled as it improves the signal-to-noise ratio (SNR) and thus allows for a smaller readout voltage $V_{\rm AC}$.

Figure 2.3 shows the temperature as function of $V_{\rm AC}$, as well as the equivalent power from the calibration performed in Figure 2.2. The expected Ohmic behavior is evident, resulting in a resistance of $R=16.9\,{\rm k}\Omega$. We can conclude that for $V_{\rm AC}<100\,{\rm mV}$, heating from the positioner readout is negligible, which is a regime where the SNR of the measurement is reasonable.

2.2 Electron temperature

In the previous section, I discussed various sources of heating of the cryostat temperature measured at the mixing chamber plate using a commercial resistive thermometer. An arguably more relevant metric for

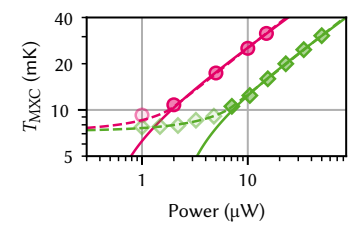


Figure 2.2: Mixing chamber temperature as function of heater (magenta) and laser (green) power. Solid lines are fits to Equation 2.2 including only the solid markers. Green dashed line is a quadratic smoothing spline fit to all laser data points. Magenta dashed line is the laser spline scaled to match the heater data with fitted factor A = 28% corresponding to the fraction of laser power absorbed and non-radiatively emitted.

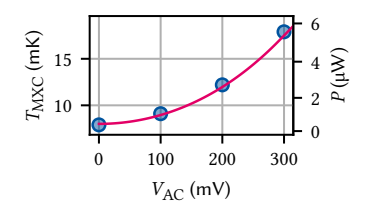


Figure 2.3: Mixing chamber temperature as function of nanopositioner AC readout voltage. The secondary axis indicates the conversion from $T_{\rm MXC}$ to power obtained in Figure 2.2 which is approximately linear in this regime, leading to the expected $P \sim R^{-1}V_{\rm AC}^2$ behavior. Solid line is a fit to the power with $R = 16.9 \, {\rm k}\Omega$.

quantum device experiments is the electronic temperature which – depending on how it is measured in detail - corresponds to the temperature of the Fermi distribution of electrons in or coupled to a reservoir rather than the temperature of the crystal lattice. Precisely because the behavior of these quantum devices depends so sensitively on the electron temperature, one can also flip this relationship on its head and use them to measure the temperature, an instance of single controlled quantum systems being used as highly sensitive probes of physical quantities known as quantum sensing [Degen2017]. Gate-defined quantum dots (GDQDs) hosted in the two-dimensional electron gas (2DEG) of a semiconductor heterostructure offer several different ways of measuring the electron temperature that are each different in subtle ways. For example, using an adjacent charge sensor, one can measure the width of a lead³ transition [Maradan2014] or the width of the inter-dot transition in a double quantum dot (QD) [DiCarlo2004]. Simpler still, one can measure the width of a Coulomb resonance in the conductance through a QD [Ihn2009, Maradan2014]. All of these methods rely on some form of energy reference scale that relates the energy of an electron confined in a QD to some externally controlled parameter such as a voltage, however. Typically this is the so-called *lever arm* α , which is the constant of proportionality between the plunger gate voltage and the electrochemical potential μ_N for adding the *N*th electron to the quantum

dot [Ihn2009]. It can be measured using pulsed-gate spectroscopy [Fujisawa2001, Harbusch2010], photon-assisted tunneling [Kouwenhoven1994], or using bias spectroscopy (Coulomb diamonds) [Kouwenhoven2001, Ihn2009].

Here, I chose the simplest of these techniques that require the least tuneup to avoid unnecessarily complicating things. That is, I formed a single QD in a gated GaAs/AlGaAs heterostructure and extracted the lever arm from Coulomb diamonds and the electron temperature from the conductance trace of a Coulomb resonance at zero bias in the sequential tunneling regime. The gate layout of the device used is shown in Figure 2.4. Designed for two-qubit experiments with two-electron spin qubits by **Cerfontaine2019**, I tuned the device to host a single large QD in the center of the device. The gates are color-coded according to the voltages applied with the device in the few-electron regime. I applied a bias voltage at the Ohmic contact situated to the right of gate SA using a DecaDAC voltage source and measured the current at the Ohmic contact to the left of gate SD using a Basel Precision Instruments SP 983c I/V converter with non-inverting input shorted to ground.⁴ Gate voltages were also supplied by the DecaDAC, divided by six and low-pass filtered at room temperature in the break-out box (BOB). All but the four long gates (RFA-RFD) coming in from the top of the device were connected to the filtered DC lines as described in Reference **Descamps2021**. The former were connected to RF lines attenuated with 20 dB, 6 dB, 0 dB and 3 dB attenuators mounted to the PT2, Still, Cold, and MXC plates, respectively, and connected to a Zurich Instruments HDAWG but unused during these experiments.

To tune the electrochemical potential in the dot, I set up a virtual plunger gate [Botzem2018] from a linear combination of the gates NBC and TBC by performing a two-dimensional sweep of TBC against NBC. From the slope m of a charge transition in the voltage space spanned by TBC and NBC, I computed the weights of the virtual gate in terms of the physical gates as

$$V_{\rm p} = \frac{1}{\sqrt{1+m^2}} ({\rm TBC} + m \times {\rm NBC}).$$
 (2.4)

Following this procedure, even a dot that does not lie in the middle be-

3: A "lead" is a reservoir of charge carriers coupled to a quantum dot.

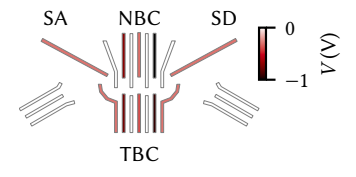


Figure 2.4: Gate layout of a quadruple quantum dot with two charge sensor QDs from Reference Cerfontaine2019. Ohmic contacts used for transport measurements are right (left) of SA (SD). The gates are colored according to the voltages applied with the device hosting a single large QD in the few-electron, sequential tunneling regime.

4: I use the same naming scheme for gate electrodes as Reference Cerfontaine 2019.

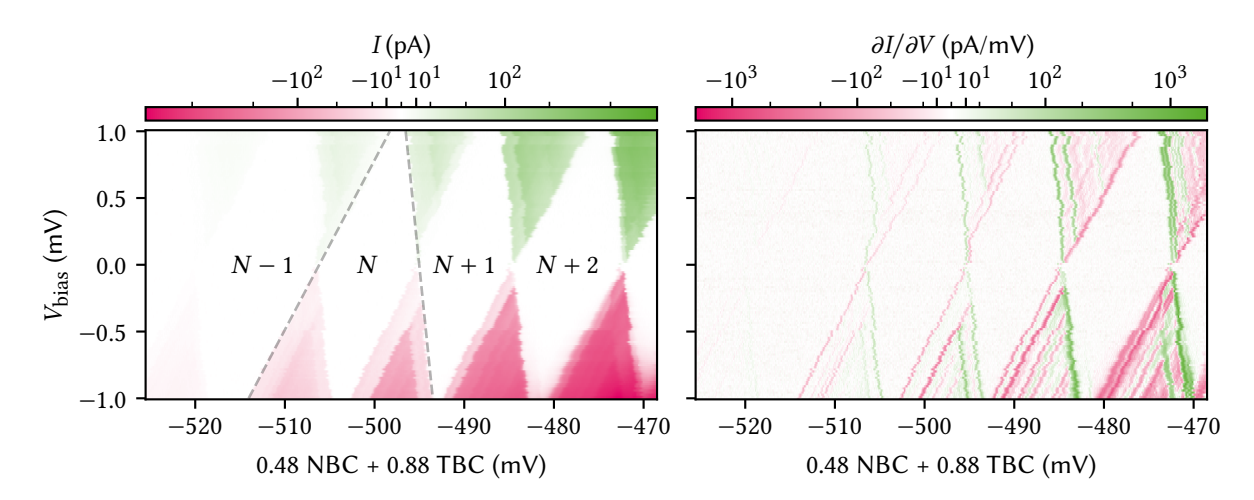


Figure 2.5: Coulomb diamond measurement of the single GDQD confined by applying static voltages to the gates shown in Figure 2.4. The left panel shows the current measured with a transimpedance amplifier (TIA) with a bias applied on one side of the device. The horizontal axis shows the virtual plunger gate swept for each bias voltage indicated on the vertical axis. The difference in slope of the dashed gray lines around the N-electron diamond yields the lever arm α converting virtual plunger gate voltage to (relative) energy inside the dot. From the fact that the slopes are not equal up to a sign we can infer that the coupling to source and drain reservoirs is unequal also, indicating that either the dot is situated closer to SA than to SD, or the topology of the tunneling contacts in the 2DEG is different due to different electrostatic potential. The right panel shows the differential conductance obtained from differentiating the data from the left panel along the plunger gate axis. Clearly visible are several additional transition lines which correspond to excited states inside the dot becoming energetically available within the bias window.

tween the two gates, *i.e.*, couples more strongly to one than the other gate, should not move in position when changing the virtual gate voltage. Having set up the virtual plunger gate, I performed a Coulomb diamond measurement wherein the (virtual) plunger gate is swept as the sourcedrain bias voltage is varied [Ihn2009].⁵ The left panel of Figure 2.5 shows the current of the Coulomb diamond measurement. Starting from zero bias, when current can only flow through the Coulomb-blockaded QD when both source and drain are aligned with an energy level in the dot, increasing the bias voltage opens up the *bias window*, allowing current to flow as long as the dot's energy level is inside the window. This defines areas of zero (blockaded) current within the space of plunger and bias voltage that takes on the shape of a diamond whose height (along the bias axis) is given by the energy penalty of adding another electron to the dot [Ihn2009],

$$E_{\rm add} = \mu_{N+1} - \mu_N = E_c + \Delta E,$$
 (2.5)

where μ_N is the electrochemical potential of the dot with N electrons, E_c is the charging energy due to Coulomb repulsion, and ΔE is the single-particle energy spacing. At the same time, the width of a diamond (along the gate voltage axis) is given by

$$\Delta V_{\rm p} = \alpha^{-1} E_{\rm add},\tag{2.6}$$

implying that we can extract the lever arm α from the geometry of the diamonds. Drawing lines with slopes m_1 and m_2 along the onsets and offsets of current through the Coulomb resonance at zero bias (dashed gray lines), I obtained

$$\alpha = |\Delta m| = |m_1 - m_2| \approx 0.11 \,\text{eV/V}.$$
 (2.7)

Although not of particular interest for the electron temperature, a Coulomb

5: In this case, the source-drain bias is asymmetric as the drain is always grounded and only the electrochemical potential of the source reservoir is changed. This does not qualitatively change the physics of the measurement, though.

diamond measurement can also be used for excited state spectroscopy. Computing the differential conductance $\partial I/\partial V_{\rm p}$ makes visible a host of additional transition lines in the conducting region of the map (right panel of Figure 2.5).⁶ These correspond to excited states of the quantum dot entering the bias window. Their sign depends on the tunnel coupling of the state to source and drain [Ihn2009].

Having measured the energy reference scale, the lever arm α , I proceeded to measure the conductance through a single Coulomb resonance as function of virtual plunger gate voltage $V_{\rm p}$ in order to measure the electron temperature. The line shape of such a resonance is qualitatively different in two limiting regimes of two competing energy scales, the tunnel coupling Γ of the quantum dot to the leads and the thermal energy $k_{\rm B}T$. If the former dominates transport through the QD is said to be in the resonant (coherent) tunneling regime while if the latter dominates, it is said to be in the sequential (incoherent) tunneling regime [Ihn2009]. For resonant tunneling, the line shape has the form of a Lorentzian of width Γ . For sequential tunneling, the line shape of a resonance at $V_{\rm p}^{\rm res}$ is given by

$$G(V_{\rm p}) = \frac{e^2}{2h} \frac{\Gamma}{4k_{\rm B}T} \cosh^{-2} \left[\frac{\alpha \left(V_{\rm p} - V_{\rm p}^{\rm res} \right)}{2k_{\rm B}T} \right]$$
 (2.8)

in linear response (small bias). Thus, I tuned the device to small tunnel couplings (high tunnel barriers) and measured $G(V_{\rm p})$ with a small bias voltage. The resulting conductance trace is shown in Figure 2.6 together with a fit to Equation 2.8. From the fit we can extract the parameters $T=74.9~{\rm mK}$ and $\Gamma=0.524(5)~{\rm \mu eV}=6.08(6)~{\rm mK}$, confirming the sequential tunneling regime of $\Gamma\ll k_{\rm B}T.^7$

6: Features inside the blockaded region can also occur, indicative of cotunneling.

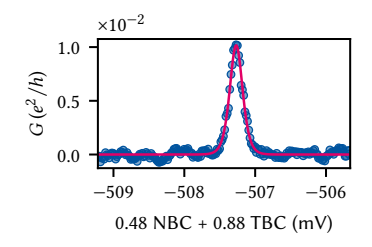


Figure 2.6: Conductance of a Coulomb resonance in the sequential tunneling regime. Magenta line is a fit to Equation 2.8 with $T=74.9\,\mathrm{mK}$ and $\Gamma=0.524(5)\,\mathrm{meV}$.

7: In a different tuning state of the device, the conductance would also sometimes change sign close to the resonance at small biases. The line shape in this configuration was well described by source and drain reservoirs at different temperatures,

$$G(V_{\rm p}) \propto f(V_{\rm p} - V_{\rm p}^{\rm res,S}) - f(V_{\rm p} - V_{\rm p}^{\rm res,D}), \label{eq:GVp}$$

with the Fermi-Dirac distribution

$$f(V) = \left[\exp(\alpha V/k_{\rm B}T) + 1\right]^{-1}$$

The precise physical mechanism behind this behavior is not understood.

HE confocal microscope integrated into a millikelvin-temperature cryogen-free DR accommodating free-space optical measurements together with DC and AC electrical control was designed and set up by **Descamps2024** [**Descamps2021**, **Descamps2024**]. In this chapter, I lay out improvements to the design to improve the optical efficiency of the microscope. I review the relevant relationships between optical parameters, estimate the maximum expected efficiency, and compare it to measurements. Furthermore, I characterize the cross-polarization extinction and outline various schemes I established to automatically control the motorized stages regulating the excitation power and rejection as well as the diffraction grating spectrometer and charge-coupled device (CCD). Lastly, I demonstrate the setup's efficacy to measure photon anti-bunching in a $g^{(2)}$ measurement on self-assembled quantum dots in InGaAs.

3.1 Light coupling

While the microscope arrangement on top of and inside the cryostat is free space optics to enable imaging of the sample, illumination and collected light are routed to and from the optical table using SMFs. Convenience aside, for the illumination this is a natural choice since the guiding mode of these fibers very closely approximates the fundamental TEM_{00} laser mode [Kowalevicz2006]. For the collected light, it is less obvious that a SMF is the best choice. Coupling light - of any mode profile in and out of fibers invariably incurs losses. Because of the small mode field diameters on the order of a few micrometers, aligning the optics for coupling is a sensitive task and subject to external disturbances such as vibrations (cf. Chapter 4). Moreover, even for perfect mode matching and alignment, there are reflection losses on the percent level. In Subsection 3.1.2, I discuss the coupling of collected light into the SMF in more detail. Despite these loss mechanisms, the single-mode character of the detection fiber is crucial to the microscope's operation because the cross-polarization extinction critically relies on the spatial filtering of the reflected mode by the fiber [Benelajla2021, Steindl2023]. I discuss the cross-polarization extinction in more detail in Subsection 3.1.4.

3.1.1 Choosing lenses

Figure 3.1 shows a sketch of the free space optical path. There are three lenses that need to fulfil different tasks. First, the excitation ocular (E), which collimates the Gaussian beam launched from the fiber. Next, the objective lens (O), which focuses the beam onto the sample and at the same time collects and collimates the reflected and emitted light. Finally, the collected light is focused by the detection ocular (D) into another fiber for spectral analysis. Since Gaussian beams behave fundamentally differently to geometrical optics, there are different requirements for the lens specifications. In the following, I will review the different beam behaviors and outline the rationale behind the choices made for the lenses.

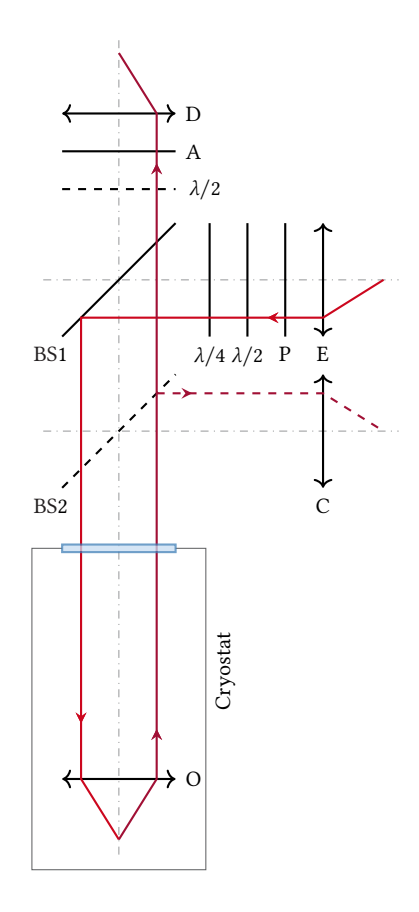


Figure 3.1: Reduced sketch of the microscope optical path. A Gaussian beam is launched from a single-mode fiber (SMF) and collimated by the excitation ocular (E). It is polarized (P), passes $\lambda/2$ and $\lambda/4$ -plates, and is reflected into the cryostat by a 90:10 beam splitter (BS). An objective lens (O) focuses the beam onto the sample and collects and collimates the emitted light. It exits the cryostat, is transmitted through the BS and an analyzer (A) before being focused into the SMF by the detection ocular (D). Another $\lambda/2$ -plate can be inserted below the analyzer to rotate the plane of polarization, and another beam splitter can be inserted below the first to divert some of the light to a complementary metal-oxide-semiconductor (CMOS) camera with ocular lens (C).

The fundamental Gaussian ${\rm TEM}_{00}$ mode has the rotationally symmetric electric field profile [Yariv1989]

$$E(\rho, z) = E_0 \frac{w_0}{w(z)} \exp\left\{-i\left[kz - \arctan\left(\frac{z}{z_0}\right)\right] - \rho^2 \left[\frac{1}{w(z)^2} + \frac{ik}{2R(z)}\right]\right\}$$
(3.1)

with the beam waist radius w_0 , the beam's 1/e-radius

$$w(z)^2 = w_0^2 \left(1 + \frac{z^2}{z_0^2} \right), \tag{3.2}$$

the wavefront radius of curvature

$$R(z) = z \left(1 + \frac{z_0^2}{z^2} \right),\tag{3.3}$$

the Rayleigh range

$$z_0 = \frac{\pi w_0^2}{\lambda},\tag{3.4}$$

and where z=0 at the beam waist as well as $\lambda=\lambda_0/n$ the wavelength in the propagating medium. For a SMF, the mode field diameter (MFD) is $2w_0$ and a beam launched from it expands according to Equation 3.2 with z=0 in its end face.

The Rayleigh range determines the the extent of the mode's near field. At $z = z_0$, the diameter of the beam is $w(z_0) = w_0\sqrt{2}$. In the far field, the beam divergence is given by

$$\theta_{\text{beam}} = \arctan\left(\frac{w_0}{z_0}\right) \approx \frac{\lambda}{\pi w_0}.$$
 (3.5)

Collimating a Gaussian beam emerging from a SMF thus requires matching θ_{beam} with the numerical aperture (NA) of the lens such that NA \geq sin θ_{beam} . Conversely, coupling a beam into a SMF requires matching the fiber's MFD to the spot size, which is constrained by diffraction. From Equation 3.5 we find, by setting $w = f \tan \theta_{\mathrm{beam}}$, the rule-of-thumb

$$w_0 \approx \frac{\lambda f}{\pi w}$$
 (3.6)

where w is the beam radius at the focusing lens.¹ For non-Gaussian beams one typically assumes a flattop profile whose diffraction pattern is given by [**Hecht2017**],

$$E(\rho) = E_0 2\pi w^2 \frac{\exp(-ikf)}{f} \frac{J_1(kw\rho/f)}{kw\rho/f},$$
(3.7)

where *w* is the radius of the lens aperture and $J_1(x)$ is the Bessel function of order one, and quotes the radius of the first Airy disk,

$$w_0 \approx 1.22 \frac{\lambda f}{2w}. (3.8)$$

Finally, let us note that the efficiency with which two electric field modes E_1 and E_2 can be matched, the *matching efficiency*, is given by the normalized spatial overlap integral [**Paschotta2005**],

$$\eta_{\rm m}(E_1, E_2) = \frac{\int dS |E_1(\rho)|^2 \int dS |E_2(\rho)|^2}{|\int dS E_1(\rho) E_2(\rho)|^2}.$$
 (3.9)

1: Note that this disregards diffraction at the aperture and is thus only a good approximation for a CA well larger than w.

Excitation path Now, for as small a spot on the sample as possible, we conclude from Equation 3.6 that we should choose an objective lens with a small focal length f_{ob} (large NA) and illuminate it with a beam with a large diameter 2w. As the lens diameter and hence the clear aperture $(CA)^2$ is constrained by the available space in the sample puck, the best lens was found to be Thorlabs 354330-B [Thorlabs354330] with $f_{\rm ob} = 3.1 \, \rm mm, \, NA = 0.7, \, and \, infinity-side \, CA = 5 \, \rm mm.^3 \, \, Having \, chosen$ the objective lens, we can next select the excitation ocular to match the beam diameter. For our typical excitation wavelengths around 800 nm, the best-matching SMF has MFD = $2w_0 = 5 \,\mu\text{m}$ [Thorlabs780HP]. Again using Equation 3.6 and solving for f, we find $f_{oc} = \pi w_0 w / \lambda \approx$ 24.5 mm when setting w = CA/2. Since w specifies the 1/e-radius of the beam, we should choose a lens resulting in a collimated beam diameter that is smaller than the CA, i.e., a shorter focal length. The lens that best matches this requirement is Thorlabs A280TM-B [ThorlabsA280TM] with $f_{\rm oc}=18.4\,{\rm mm}$, resulting in a collimated beam diameter of $2w\approx3.8\,{\rm mm.}^4$ Collimating the Gaussian beam launched from a SMF may be viewed as transforming the beam waist $w_0 \rightarrow w$, implying that the Rayleigh range after collimation is $z_0 \approx 14 \,\mathrm{m}$ (Equation 3.4), and the objective lens at a distance of $z \sim 1.5 \,\mathrm{m}$ is well in the beam's near field with negligible divergence (cf. Equation 3.2). With the beam diameter and focal lengths set, we can compute the expected spot size to be $2w_0 \approx 0.84 \,\mu\text{m}$. In Subsection 3.1.3 and Section 4.3, I compare this value to measurements.

We have thus far addressed illumination of the sample with Gaussian laser light. What now remains to deal with is the reverse direction; that is, collection of the emitted photoluminescence and focusing it into a SMF using the detection ocular lens ("D" in Figure 3.1). Before turning our attention to that task, let us briefly compare the expected performance with the lenses chosen here to those chosen in Reference **Descamps2021**. There, the ocular lens had a focal length of $f_{\rm oc}=6.2\,{\rm mm}$ and the objective lens $f_{\rm ob}=4.51\,{\rm mm}$. With these parameters, we obtain a beam diameter of $2w\approx 1.3\,{\rm mm}$ just after collimation and a Rayleigh range of $z_0\approx 1.5\,{\rm m}$, implying that the beam broadens by $\sim \sqrt{2}$ by the time it arrives at the objective lens $z\sim 1.5\,{\rm m}$ away. This would result in a spot size of $2w_0\approx 1.3\,{\rm \mu m}$, roughly a factor of two larger than with the lenses we chose here.

Detection path To choose an appropriate lens for focusing light into the SMF for spectroscopic analysis, the detection ocular ("D" in Figure 3.1), let us assume that the objective lens is fully illuminated by the emitted light. This results in a beam with diameter corresponding to the infinityside CA of the objective lens. Further neglecting beam divergence, we must then choose the focal length of the ocular such that the diffractionlimited spot size matches the MFD of the SMF. Taking the beam to have a flattop profile, an assumption that I test more closely in Subsection 3.1.2, the radius of the first Airy disk is given by Equation 3.8. For the objective lens chosen in the previous paragraph, inverting that equation leads to $f \approx 12.8 \,\mathrm{mm}$. However, the first Airy disk includes slightly less of the total power than the $1/e^2$ diameter of a Gaussian beam (cf. Equation 3.1) corresponding to the SMF's MFD. I therefore chose a slightly larger focal length, leading to the same lens as used for the excitation ocular, Thorlabs A280TM-B with $f_{\rm oc} = 18.4 \, \rm mm$ and resulting in a mode matching efficiency for a hypothetical flattop beam of $\eta_{\rm m} = 78 \, \%.5$ Again comparing the lens chosen here with that by Reference Descamps2021 with $f_{\rm oc} = 6.2$ mm, we find that we expect only $\eta_{\rm m} = 13$ % of a flattop beam's

- 2: The clear aperture (CA) is the diameter over which the lens specifications hold. Outside this diameter, light may still be transmitted but is not guaranteed to behave according to the lens design.
- 3: A lens with even higher NA exists [LightPath355330] but I found it to have too short a working distance (WD) to put our flip-chipped samples into focus. Samples with a different mounting strategy might benefit from the slightly increased focusing power of that lens.
- 4: A lens with larger focal length and hence wider beam diameter and resulting smaller spot size exists [LightPath354850] but its design wavelength is further off from our typical working wavelengths. It is also unmounted, making its integration into the optical head more cumbersome.

^{5:} Numerical optimization of the mode overlap given by Equation 3.9 for Equations 3.1 and 3.7 results in $f_{\rm oc}=21.6$ mm and $\eta_{\rm m}=82$ %, indicating the choice fits quite well

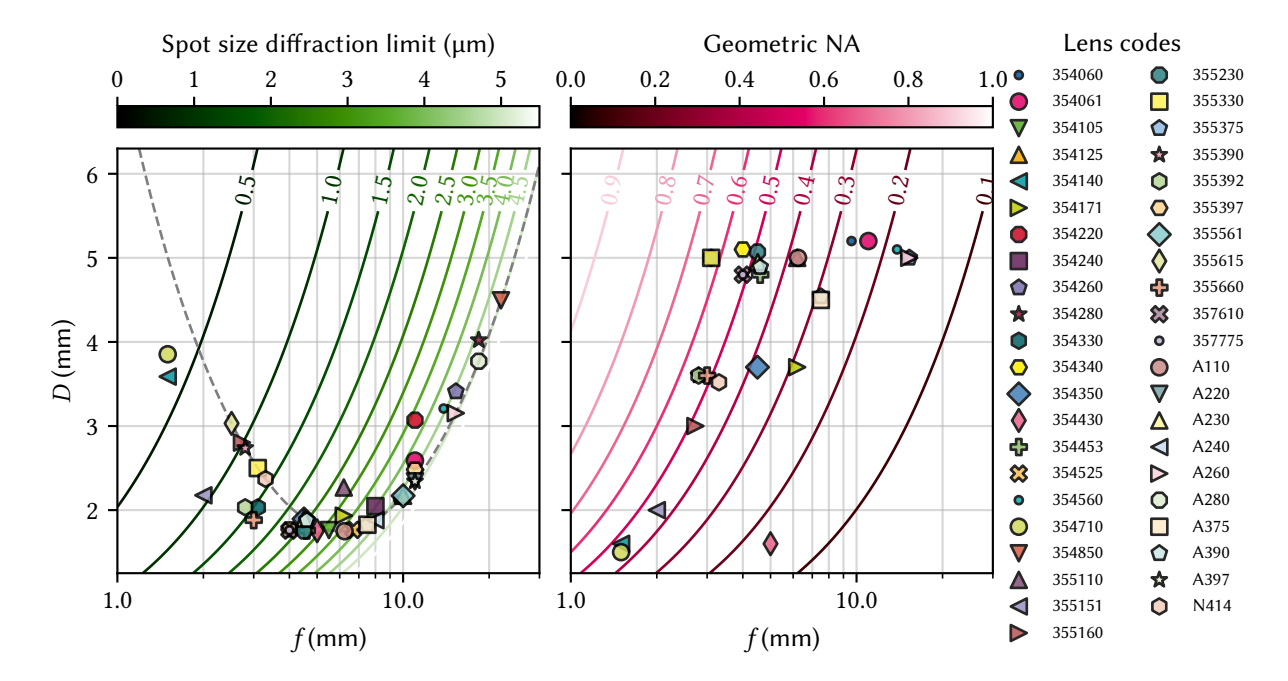


Figure 3.2: Performance of selected lenses from the Thorlabs and Edmund Optics catalogs for Gaussian (left) and geometric (right) optics. The left panel shows the diameter D of a Gaussian beam launched from a SMF with MFD = 5 μ m and collimated by the given lens at the position z = 1.5 m behind the lens plotted for various lenses. For lenses with different clear apertures on both sides, I assume a magnification of the beam by their ratio, resulting in the deviation from the theoretical beam diameter shown as a dashed gray line for some lenses, but note that this is a rough approximation for lens underfulling in particular. The green contours show the theoretical spot size diffraction limit, $2w_0$ (Equation 3.6), for a beam with diameter 2w = D. To the left of the minimum of the (apparent, note the logarithmic scale) parabola, the beam diameter increases with shorter focal length because the beam divergence after the collimating lens becomes relevant as the objective lens plane moves into the beam's far field. The right panel shows the same lenses, this time plotting their (larger, if different) CA diameter D as well as the geometric NA calculated as NA = $\sin \arctan(D/2f)$ (magenta contours).

intensity focused onto the fiber end face to couple into the fiber's TEM_{00} mode

The above considerations for choosing lenses are visualized in Figure 3.2, which plots selected lenses from the Thorlabs and Edmund Optics catalog for different scenarios to help selecting models for a specific task. The left panel deals with Gaussian optics and plots the collimated beam diameter D of a Gaussian beam launched from the SMF, collimated by the given lens, and monitored at a distance of $z = 1.5 \,\mathrm{m}$ behind it. This takes into account beam expansion due to diffraction, which depends on the focal length of the collimating lens and results in the non-monotonous dependence D(f). The contours indicate the expected spot size of the beam when the objective lens is illuminated by a beam of diameter D. The right panel deals with geometric optics and plots the NA computed from the CA diameter D and the focal length as NA = $\sin \arctan(D/2f)$. To choose a pair of collimating and objective lenses, first pick the former from the left panel. Then choose an objective lens from the right panel to suit the focusing power needs. Identifying the objective lens in the left panel and drawing a vertical line from its focal length and a horizontal line from the collimator's beam diameter gives the expected spot size of the beam where the two lines cross.

Having picked the lenses defining the characteristics of the microscope, let us now take a closer look at the expected efficiency.

6: Note that for high NA, this value can deviate from the value quoted by the manufacturer.

3.1.2 Collection efficiency

In a confocal microscope geometry, light is collected using the same lens that is also used for illumination of the sample. For excitation with a Gaussian laser beam but non-Gaussian radiation being emitted, this means that two different beam behaviors need to be matched, a task that is likely not possible to achieve completely. In the case of photoluminescence in a pristine semiconductor quantum well (QW), the optical interband transitions are well described by in-plane dipole matrix elements [Gu2013]. If, on the other, the light emerges from a photonic crystal cavity (PCC), the far field pattern is close to a Gaussian mode and the considerations below need to be adjusted accordingly [Wu2024]. Here, I discuss dipole emission from the QW, which needs to be coupled into a SMF with near-Gaussian mode profile, invariably resulting in losses. A detailed analysis of the electric field profile to compute the expected coupling efficiency from the sample into the SMF is beyond our scope here as it would require taking into account the full sample and lens geometries as well as diffraction, a task only possible by employing a fullfledged numerical optics simulation suite. However, we can make some crude simplifications of the problem to estimate the order of magnitude of these effects. To this end, I model the light source as a point dipole beneath the surface of a homogeneous slab of dielectric material and the real lenses as ideal thin lenses.

Consider the situation sketched in Figure 3.3. A dipole p oriented along x in the plane of a GaAs QW with refractive index n buried at a depth d beneath the surface of the sample emits light into the halfspace above it. In spherical coordinates (r, ϑ, φ) oriented along x, that is, embedded in the cartesian coordinate system (y, z, x), the emitted radiation has the field components [Griffiths2017]

$$\mathbf{E}(r,\vartheta) = A(r) \left[E_r(r,\vartheta) \hat{\mathbf{e}}_r + E_{\vartheta}(r,\vartheta) \hat{\mathbf{e}}_{\vartheta} \right]$$
(3.10)

$$\mathbf{H}(r,\vartheta) = \frac{\epsilon}{\mu} A(r) H_{\phi}(r,\vartheta) \hat{\mathbf{e}}_{\phi}$$
 (3.11)

with

$$A(r) = \frac{|\mathbf{p}|k^2}{4\pi\epsilon} \frac{\exp(ikr)}{r}$$
(3.12)

$$A(r) = \frac{|\mathbf{p}|k^2}{4\pi\epsilon} \frac{\exp(ikr)}{r}$$

$$E_r(r,\theta) = \left(\frac{2}{k^2r^2} - \frac{2i}{kr}\right)\cos\theta$$
(3.12)

$$E_{\theta}(r,\theta) = \left(\frac{1}{k^2 r^2} - \frac{i}{kr} - 1\right) \sin \theta \tag{3.14}$$

$$H_{\phi}(r,\theta) = -\left(\frac{i}{kr} + 1\right)\sin\theta \tag{3.15}$$

and where $\theta = \arctan(\sqrt{z^2 + y^2}/x)$, r is the distance from the point dipole, and $k=2\pi/\lambda=2\pi n/\lambda_0$ and $\epsilon=\epsilon_{\rm r}\epsilon_0$ are the wavenumber and the permittivity in the medium, respectively. Since kr is of order unity at z = 0, the semiconductor surface is in the dipole's intermediate-field regime where all terms contribute roughly equally.

The emitted light is refracted at the surface and we collect and collimate it with an objective lens (labeled "O") with NA = $\sin \theta_{\rm m}'$ at distance $f_{\rm ob}$ above the surface of the sample, where $f_{\rm ob}$ is the focal length and $\theta_{\rm m}'$ the angle of the marginal ray. The NA determines the maximum amount of light the objective lens can collect, and using Snell's law we can relate the angle of a ray outside the sample θ' to the angle inside the sample

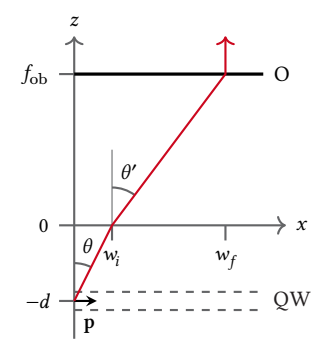


Figure 3.3: Sketch of a light source located inside a dielectric medium (z < 0, n > 1) emitting light in the upwards direction to collection by an objective lens in air (z > 0, n = 1). The red line indicates the marginal ray of the lens with focal length $f_{\rm ob}$ and CA 2w.

$$\theta = \arctan(\sqrt{x^2 + y^2}/z),$$

$$\sin \theta' = n \sin \theta,$$
(3.16)

with $n \approx 3.57$ at $\lambda_0 = 800$ nm and T = 0 K. This yields $\theta_{\rm m} = \arcsin({\rm NA}/n) \approx 11^\circ$ for the emission angle of the marginal ray inside the semiconductor, implying that only a small fraction of light escapes the sample. Indeed, according to Poynting's theorem the radiated power through the surface Σ is given by

$$\langle P \rangle = \int_{\Sigma} d\Sigma \cdot \langle S(r, \theta) \rangle$$
 (3.17)

with the time-averaged Poynting vector

$$\langle \mathbf{S}(r,\vartheta) \rangle = \frac{1}{2} \operatorname{Re}(\mathbf{E}(r,\vartheta) \times \mathbf{H}^*(r,\vartheta)).$$
 (3.18)

As I show in Section A.1, the fraction of the power radiated into the cone $\theta \in [0, \theta_{\rm m}]$ able to be collected by the objective lens, the *collection efficiency*, is thus

$$\eta_{\rm c} = \frac{1}{2} - \frac{1}{8n^3} \left(4n^2 - NA^2 \right) \sqrt{n^2 - NA^2} \approx 1.4 \,\%$$
(3.19)

with NA = 0.7 for the chosen objective lens (cf. Subsection 3.1.1).

In order to estimate the fiber coupling efficiency of the light escaping the sample and collected by the objective lens focused by the ocular lens "D", we need to consider refraction and transmission of the electric field at the surface, collimation by the objective lens, as well as diffraction at the ocular lens aperture. A detailed accounting of these effects is beyond the scope of this thesis. However, let us at least gain an intuition for the degree of these effects. Since we observe the dipole, oriented in-plane inside the QW, from the side, it is useful to rotate the spherical coordinate system so that it is embedded in the coordinate system (x, y, z) as defined in Figure 3.3 with coordinates (r, θ, ϕ) .

The magnitude of the electric field vector in the surface plane, which I derive in more detail in Section A.2, is shown in the upper panel of Figure 3.4. The circle delimits the cone of emission bounded by $\theta_{\rm m}$ (radius w_i) while the arrows indicate the projection of the electric field E(x, y, z)onto the interface, indicating that the polarization in the plane points mostly along yat this distance from the source. Accounting for refraction and modifying the perpendicular and parallel (s and p) components of the electric field according to Fresnel's equations [Hecht2017] results in the electric field in the plane of the objective lens at a distance of $f_{\rm ob}$ shown in the lower panel. Here, the circle indicates the CA of the lens with radius w_f . The picture is quite different from before. First, the field is almost exclusively polarized along x, the dipole axis, as we might have expected. Moreover, the intensity $\propto |E|$ does not depend strongly on the azimuthal angle ϕ at this distance, allowing us to approximate the field as rotationally invariant to estimate the coupling efficiency into the SMF.⁷ As shown in Section A.2, the field after collimation is thus to good approximation given by

$$\mathbf{E}(r,\theta) = \tilde{A}(r)E_r(\theta) \tag{3.20}$$

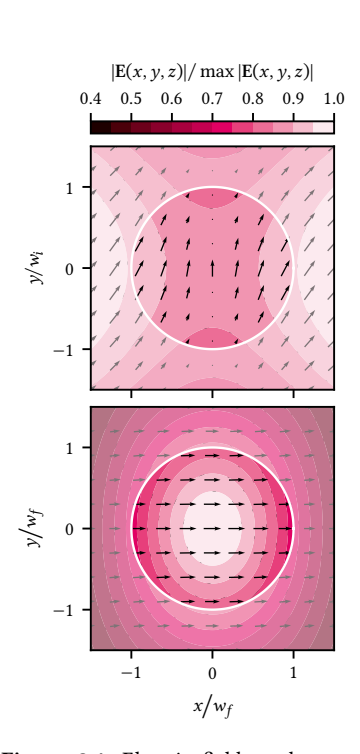


Figure 3.4: Electric field at the sample surface (top) and the objective lens plane (bottom). The white circle indicates the area from which light can be collected, corresponding to the marginal angle $w_i = d \tan \theta_{\rm m}$ for the upper and $w_f = {\rm CA}/2$ for the lower plot. The arrows represent the projection of the vector-valued electric field onto the xy-plane. At the interface, the polarization is mostly out-of-plane and along y, but in the far field, represented by the lens plane, it is almost perfectly polarized along x. The intensity profile changes from a local minimum at the center to maximal with a roughly circular dependence.

7: Note that, while a fairly good approximation for the amplitude, this is likely not a good approximation for the phase because $kw_i \sim 1$, meaning that when the light exits the sample the phase is not

with

$$\tilde{A}(r) = \frac{|\mathbf{p}|k^2}{4\pi\epsilon} \frac{\exp(ikz)}{r} \tag{3.21}$$

$$\tilde{A}(r) = \frac{|\mathbf{p}|k^2}{4\pi\epsilon} \frac{\exp(ikz)}{r}$$

$$E_x(\theta) = \frac{2n\pi\cos\theta\left[\cos\theta + n\nu(\theta) + n\nu(\theta)\cos\theta + \nu(\theta)^2\right]}{\left[n\cos\theta + \nu(\theta)\right]\left[\cos\theta + n\nu(\theta)\right]}$$
(3.21)

and where $v(\theta) = \sqrt{1 - n^2 \sin^2 \theta}$. For $\tilde{A}(r)$, we assumed a perfect lens that transforms a spherical wave front with constant phase at constant *r* into a plane wave with constant phase at constant z.

The radial intensity profile ($\rho = f_{\rm ob} \tan \theta$ and $r = \sqrt{\rho^2 + f_{\rm ob}^2}$) given by the absolute value square of Equation 3.20 is shown in the upper panel of Figure 3.5 together with a flattop (magenta) and a Gaussian (green) beam profile for comparison. The intensity drops to about half its maximum at the edge of the lens aperture, $\rho = w$. We may thus expect the mode matching to be qualitatively different from the flattop behavior discussed previously when coupling this beam into a SMF with a guiding mode very closely approximating the Gaussian TEM_{00} mode.

The light collected and collimated by the objective lens next passes through the ocular lens in the detection arm which focuses it into the SMF. The image of the beam on the fiber end face is given by the Fraunhofer diffraction pattern generated by the wave (Equation 3.20) incident on the ocular lens aperture, which I give in Section A.3. The resulting diffraction pattern, Equation A.28, scaled with the radius ρ is plotted in the middle panel of Figure 3.5 together with the corresponding Airy disk result for a flattop beam (Equation 3.7) and the SMF's guiding Gaussian mode. The pattern of the flattop and the more accurate mode profile from Equation 3.20 are quite similar, but noticeably differ from the Gaussian mode at higher radii ρ. The lower panel shows the fraction of power included in a circle of radius ρ , $P(\rho) \propto \int_0^{\rho} d\rho' \; \rho' I(\rho')$, demonstrating that we can expect the mode matching to be fairly good. Indeed, evaluating Equation 3.9 for the light field (E_l , Equation 3.20) and the fiber's guiding mode (E_g , Equation 3.1), results in

$$\eta_{\rm m}(E_{\rm l}, E_{\rm g}) \approx 83\% \tag{3.23}$$

for our parameters, slightly better than the naive result using the flattop beam. Together with the collection efficiency (Equation 3.19) and accounting for the transmittivity of the BS, $T \approx 87\%$, the optical efficiency [Sze2007] from sample to fiber is thus

$$\eta_{\rm o} = \eta_{\rm c} \eta_{\rm m} T \approx 1.0 \%. \tag{3.24}$$

3.1.3 Imaging the laser spot

As the confocal microscope is free space, we are in a position to image the sample using a white light source. We can also, though, use the imaging capabilities to inspect the laser spot focused onto the sample and compare it to the behavior expected from Subsection 3.1.1. To this end, I coupled the laser into both excitation and detection arm of the microscope and aligned their spots on top of each other on a gold gate fabricated using optical lithography - ensuring close to perfect reflectivity by monitoring their image on the Thorlabs DCC1545M CMOS camera (cf. Figure 3.1). A feature of known size, for example the width of the gate, can be used to calculate the magnification of the lens system defined by O and C (cf. Section 4.3). Once aligned and blocking the beam from each

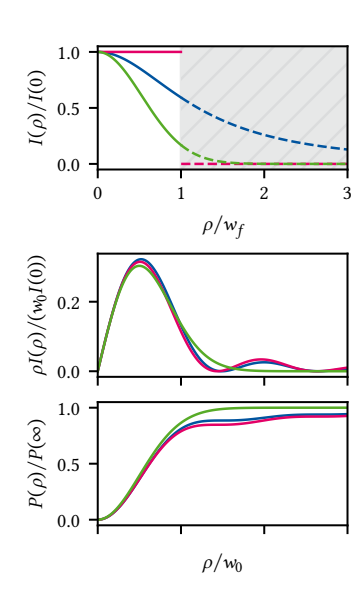


Figure 3.5: Electric field modes. Top: mode intensity of the light collected from the semiconductor at the objective lens plane (blue) in comparison to a flattop (magenta) and Gaussian TEM₀₀ mode with theoretical beam diameter after collimating with the ocular lens (green). w_f is the lens CA radius. Middle: diffraction pattern of the collimated beam when focusing onto the SMF end face with the ocular lens (blue), the flattop approximation (magenta), and the fiber's guiding mode (green). The curves are scaled with the radial coordinate ρ to highlight the Airy rings. Bottom: power encased by a circle with radius ρ , $P(\rho) \propto$ $\int_0^{\rho} \mathrm{d}\rho' \; \rho' I(\rho').$

- 8: While the specifications of the beamsplitter are T: R = 90%: 10%, in reality $T: R \approx 87\%: 6\%$ which also varies slightly with polarization.
- 9: Note that this varies slightly depending on the focal distance of sample and camera from their respective lenses. Theoretically, we expect the magnification to be given by the ratio of their focal lengths, $M = f_{\rm oc}/f_{\rm ob} \approx 32$.

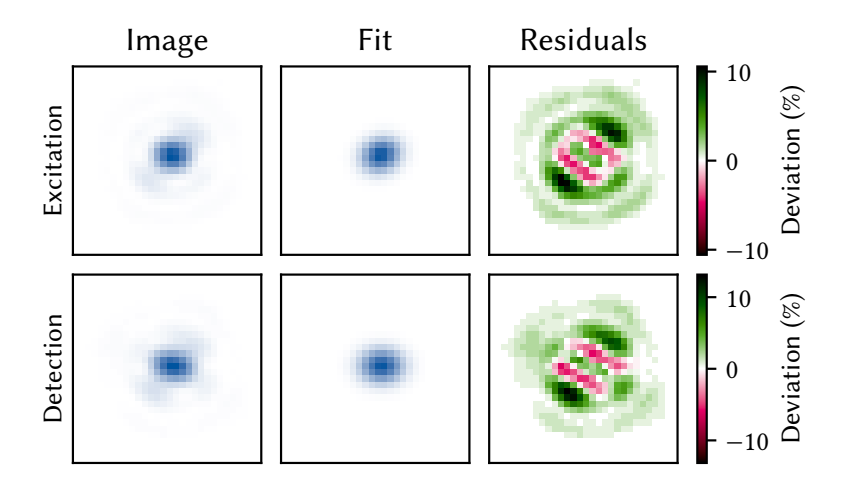


Figure 3.6: Imaging of the laser spots using the free-space imaging capabilities of the confocal microscope. Left column shows images of the spot on an optical gate taken with the CMOS camera, while the middle column shows the fit to Equation 3.25 rotated by a variable amount. Right column shows the residuals of the fit, highlighting non-Gaussian components in the beam. Top row is the excitation, bottom the detection path.

arm in turn, I recorded a picture of the spots.

From Equation 3.1, we can deduce that a perfect, aberration-free spot would have the two-dimensional intensity distribution

$$I(x,y) = I(0,0) \exp\left\{-\frac{2x^2}{w_{0,x}^2} - \frac{2y^2}{w_{0,y}^2}\right\},\tag{3.25}$$

where $w_{0,\{x,y\}}$ are the beam waist radii in x and y-direction, respectively, which are equal in the perfect case and introduce ellipticity else. Allowing for ellipticity as well as a rotation of the coordinate system with respect to the axes of the CMOS camera, we can fit Equation 3.25 to the pictures obtained previously. The result is shown in Figure 3.6 for the excitation path in the upper and the detection path in the lower row. The first column shows a cropped section of the recorded images, showing good alignment between both spots but also some sidelobes along perpendicular axes rotated by around 45° to the camera axes. This is also reflected in the relative residuals of the fitted spot that clearly shows that the spot is not described only by a Gaussian TEM_{00} mode. However, extracting the beam waist radii from the fits and scaling with the magnification factors, which display a slight asymmetry between the two axes, 30 to 27.4, we obtain reasonable results between 1.4 and 2 times larger than the diffraction limit given by the lens geometries, cf. Subsection 3.1.1, as shown in Table 3.1. For a more faithful measurement of the spot size one typically performs a knife-edge measurement. This has the advantage that it does not depend on additional components of the optical path such as the beam splitter BS2 and focusing lens. In Section 4.3 I perform such a measurement in the context of vibration spectroscopy.

From experience, the sidelobes present in Figure 3.6 can be suppressed with better alignment and are most likely due to an imperfect focal distance of the fiber collimating lenses D and E resulting in a secondary (back) focal plane before the objective lens. The asymmetry resulting in elliptical spot cross sections, on the other hand, might be due to several factors including a tilt of the sample or alignment of the imaging arm of the microscope. Finally, note that the excitation spot typically looks worse than the detection spot, likely because of the additional optical elements introducing beam distortions.

Table 3.1: Beam waist radii extracted from the fits of Equation 3.25 to the images recorded using the imaging path of the confocal microscope.

Веам waist (µm)	$w_{0,x}$	$w_{0,y}$
Detection path	0.58	0.75
Excitation path	0.60	0.84
Diffraction limit	0.42	0.42

10: Notice that the asymmetry is due solely to the magnification factor rather than the image on the camera.

3.1.4 Cross-polarization extinction

3.2 Exemplary measurement of non-classical light

As a demonstration of the optical capabilities of the setup, I performed second-order coherence measurements of an InAs self-assembled quantum dot (SAQD) in GaAs. SAQDs are optically active quantum dots (OAQDs) that form at random locations during epitaxial growth. They have demonstrated excellent optical properties and show potential for technological applications such as quantum repeaters [Petroff2001, Warburton2013,

Lodahl2015, **Zajac2025**]. In particular, SAQDs can be operated as single-photon sources. Because they locally deform the band structure, they can capture and confine excitons. Owing to their small spatial extents, strong Coulomb interaction shifts the energy of excitonic complexes other than the neutral exciton X^0 , implying that light emitted at $hv = E_{X^0}$ upon recombination is certain to contain a single photon within a time window on the scale of the exciton lifetime. This so-called photon anti-bunching behavior can be measured with a Hanbury Brown-Twiss (HBT) interferometer and serves as a fingerprint of single-photon source behavior.

I loaded and cooled down an InAs/GaAs chip with SAQDs and selected a bright and isolated emission line. A typical PL spectrum under cw abovegap excitation is shown in Figure 3.7. The brightest line at 1.4212 eV = 872.39 nm has a width of around 15 μ eV = 12 pm close to the grating ¹² resolution limit of around 10 pm. To perform a $g^{(2)}$ experiment, light emitted by the source is spectrally filtered using the Horiba FHR1000 diffraction grating spectrometer and sent through a 50:50 BS with a Excelitas SPCM-850-14-FC single-photon counting module (SPCM) on each exit port. The clicks from the detectors are time-correlated using a counting card (Swabian Instruments Time Tagger 20), computing the second-order coherence function [Kimble 1976, Walls 1979, Cohen-Tannoudji 1998]

$$g^{(2)}(\tau) = \frac{\langle \hat{n}_1(t)\hat{n}_2(t+\tau)\rangle}{\langle \hat{n}_1(t)\rangle\langle \hat{n}_2(t)\rangle},\tag{3.26}$$

where $\hat{n}_i(t) = \hat{b}_i^{\dagger}(t)\hat{b}_i(t), i \in \{1,2\}$ is the photon-number operator for a single mode at detector i and averaging takes place over time. For a weakly excited artificial atom, one expects this function to take on the form [Walls 1979]

$$g^{(2)}(\tau) = [1 - \exp(-\tau \gamma/2)]^2,$$
 (3.27)

where γ is the Einstein A coefficient, *i.e.*, the spontaneous emission rate or inverse lifetime $1/T_1$ of the excited state.

The upper panel of Figure 3.8 shows the measurement after a total run time of around 17 h together with a fit to Equation 3.27 from which we extract a lifetime of $\gamma^{-1}=430(11)\,\mathrm{ps.}\,\,g^{(2)}(0)$ does not quite reach the theoretically expected value of zero. Likely causes include the remnant dark counts of the detectors. ¹³ and additional decay channels. The lower panel shows the same measurement for logarithmically spaced time lags τ covering a wider range. A peculiar feature shows at $\tau=13.4\,\mathrm{ns}$, where the measurement suggests a bunching of photons with $g^{(2)}(\tau)\approx 2$. The origin of this bump is not understood. One possible cause might be multiple reflections in the setup. However, in free space the delay corresponds to a time-of-flight distance of 4 m, far larger than any distances

11: Also known as sub-Poissonian statistics.

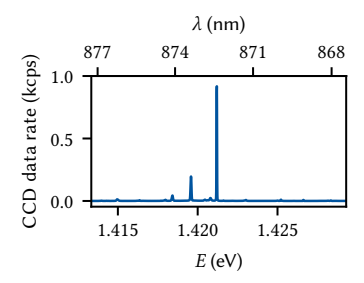


Figure 3.7: Photoluminescence (PL) spectrum of a SAQD under continuous-wave (cw) excitation at 793 nm.

12: 1800 lines/mm

check

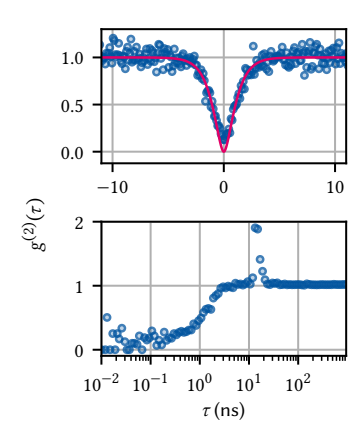


Figure 3.8: $g^{(2)}$ measurement of the emission line at 872.267 nm under cw excitation with 1 μ W at 793 nm. The monochromator bandwidth was $\Delta\lambda=200~\mathrm{pm}=325~\mu\mathrm{eV}.$

in the setup besides the path between objective and ocular lens at $\sim 1.5~\rm m$. Assuming a refractive index of n=1.4 for a typical SMF results in a characteristic distance of 2.8 m which also does not match any components in the setup. What can be said is that it is related to the setup rather than a physical process in the sample since the feature also appeared in $g^{(2)}$ measurements on different samples. For measurements such as the one performed here, though, this effect may safely be treated as a measurement artefact and ignored. Only in case the characteristic decay time γ^{-1} approached 10 ns this would need to be investigated more carefully. Finally, I note that the dependence of the integrated peak power on excitation power for this line was superlinear, suggesting an excitonic complex rather than the natural exciton as the source of emission. The line at 1.4196 eV did show a linear relationship and produced qualitatively the same $g^{(2)}$ results.

14: The closest match is the 10 m fiber from the optical head to the optical table.

Vibration noise



microscope's performance is limited chiefly by two factors; first and foremost the resolution and imaging fidelity are limited by the systematic aberrations introduced by the optics. Various types of aberrations exist, and modern microscopes usually include a complex assembly of optics to compensate for these errors. The second factor is vibration noise. This becomes more significant the higher the resolution of the microscope simply because ambient, environmental vibrations within the range of human civilization is typically on the order of $100 \, \mu \text{m/s}$ root mean square (RMS) [Gordon1999]. Comparing that to transmission electron microscopes with atomic resolution, it is clear that these instruments require purpose-built rooms to reduce the vibration level to acceptable levels.

The demands on the microscope discussed in the present thesis are fortunately much more relaxed as the features we need to resolve are on the micrometer scale. However, we face the additional challenge of ultralow temperatures, or rather the manner in which they are achieved. The microscope is integrated into a dry DR. In contrast to a wet DR, which uses a liquid Helium bath, these systems achieve the pre-cooling necessary for the ³He/⁴He dilution refrigeration cycle to work by adding a secondary refrigeration mechanism, a pulse tube refrigerator (PTR). These are closed-cycle systems that work with ⁴He compressed to ~21 bar on the high-pressure and ~7 bar on the low-pressure side. A rotating valve connecting high and low pressure lines to the cryostat in turn produces alternating gas flow inside a regenerator, where the gas absorbs heat at the low-temperature and and deposits heat at the high-temperature end [Radebaugh2009, DeWaele2011]. In commercial PTRs the frequency of the pulses of Helium gas, determined by the rotary valve motor, is usually fixed at values around 1.5 Hz.

Naturally, the compressor, the rotary valve motor, and the Helium pulses themselves introduce vibrations into the cryostat. While the cold foot of the PTR is not rigidly connected to the cryostat interior,² the entire cold head assembly rests with rubber feet on the cryostat top plate in the system's delivery status. Thus, our microscope does not only encounter passive environmental vibrations but also the active perturbation from the PTR.

[Caparrelli2006, Pelliccione2013]

This chapter is laid out as follows. In Section 4.1, I briefly discuss the theoretical underpinnings of vibration isolation to inform its optimization. To characterize and improve upon the isolation, I performed vibration noise spectroscopy using the techniques and tools presented in Part I. I employed two different approaches that I lay out in the following; first, using a commercial piezoelectric accelerometer (Section 4.2) and second, using the optical response of a spatial reflectance gradient (Section 4.3). As will become clear, the two approaches complement each other because they are sensitive to slightly different quantities.

1: Besides the limit set by the wavelength-dependent diffraction, of course.

2: In the Oxford Instruments Triton 450 copper braids connect the cold head to the PT1 and PT2 plates. There exist commercial systems that use gas exchange instead, for example the CryoConcept HEXA-DRY series [CryoConceptHexaDry].

review literature

improve

4.1 Vibration isolation

A simple yet effective method of vibration isolation is to suspend the system on passive air springs. These are typically constructed with two separate air chambers, a spring and a damping chamber, connected by pneumatic tubing. The load is rigidly mounted to a plunger that rests on a diaphragm sealing the spring chamber. Excitations of the load induce oscillations in the variable spring chamber volume. The connection to the fixed-volume damping chamber provides a flow impedance³ that manifests as a damping force to the spring chamber oscillations.

4.1.1 Damping theory

Let us adopt a simple toy model to gain an intuition for the behavior of a mass suspended on air springs as function of vibration frequency by modelling it as a damped harmonic oscillator. Consider the displacement from equilibrium x(t) of the test mass m and switch on an external perturbation u(t) acting on the base of the spring, implying that the driving force experiences both the damping rate γ and the spring stiffness $k=m\omega_0^2$ with ω_0 the resonant frequency of the undamped system. We can then compute the transfer function H(s) from the Laplace transform of the Newtonian equation of motion,

$$\ddot{x}(t) + 2\gamma [\dot{x}(t) - \dot{u}(t)] + \omega_0^2 [x(t) - u(t)] = 0, \tag{4.1}$$

yielding

$$H(s) = \frac{\hat{x}(s)}{\hat{u}(s)} = \frac{2\gamma s + \omega_0^2}{s^2 + 2\gamma s + \omega_0^2}.$$
 (4.2)

The magnitude of the transfer function evaluated at $s=i\omega$ is shown in Figure 4.1 for two different dampings, $\gamma=\omega_0/200$ (solid black line) and $\gamma=\omega_0/2$ (dashed black line). Below $\omega=\sqrt{2}\omega_0$ (vertical dotted line), external impulses are in fact amplified. The maximum at the damped system's resonance $\omega_{\rm r}=[\omega_0^2-\gamma^2]^{1/2}$ becomes smoothed out and smaller as the damping γ is increased but never drops below unity. This is the reason why resonance frequencies as small as possible are desirable in vibration isolation. Above this frequency, the system initially attenuates with 40 dB per decade up to $\omega=\omega_0^2/(2\gamma)$ and with 20 dB per decade beyond for $\gamma/\omega_0\to 0$ (the underdamped case). In the strongly damped case $(\gamma/\omega_0\to\infty)$ the attenuation is only 20 dB per decade starting at $\omega=2\gamma$.

From Equation 4.2 and Figure 4.1, we can infer two possible approaches to isolating a mass from vibrations. The first is to make the system's resonance frequency ω_0 as small as possible by resting it on a spring damping system. This maximizes the region in which external influences are attenuated. The second is to do the opposite, *i.e.*, make the entire system as stiff (large k) and thereby ω_0 as large as possible. While this minimizes the attenuation region, it also moves the amplification region close to the resonance to higher frequencies, and possibly further away from the external excitation. Consequently, this approach makes most sense if it is known that low-frequency excitations are the dominant source of vibrations.

A widely used metric for the isolation demand of vibration-sensitive equipment are the so-called vibration criteria (VCs) [Gordon1992, Gordon1999].

3: The speed of a fluid in laminar flow through a round pipe is proportional to the pressure gradient along the flow direction and to the square of the distance from the wall.

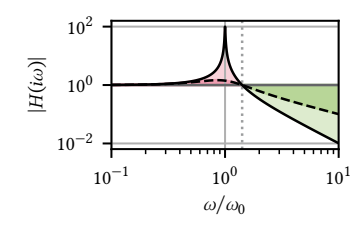


Figure 4.1: Force transmission function of a damped harmonic oscillator with $\gamma=\omega_0/100$ (solid black line) and $\gamma=\omega_0/2$ (dashed black line). Below the break frequency $\omega=\sqrt{2}\omega_0$ (dotted vertical line), external excitations are amplified (shaded red area). For larger damping γ , the amplification at resonance occurs smaller. Above $\omega=\sqrt{2}\omega_0$, excitations are attenuated (shaded green area). Both amplification below and attenuation above the break frequency become smaller as the damping rate γ is increased.

These are design standard specifications for buildings housing, for example, lithography tools. The vibration criteria (VCs) are defined in terms of band-limited RMS values similar to what I have used in the present thesis (cf. Equation 4.4 and ??). However, instead of computing the band-limited RMS with a fixed lower band edge, one uses bands of a fixed width, typically over one-third of an octave. To be specific, the one-third octave is defined in terms of its midband frequency $f_{\rm m}$ as the interval

$$f \in f_{\rm m} \times \left[10^{-1/20}, 10^{1/20}\right] \approx f_{\rm m} \times \left[2^{-1/6}, 2^{1/6}\right]$$
 (4.3)

whose bandwidth Δf is approximately 26 % larger than $f_{\rm m}$ and where the latter is defined referenced to 1000 Hz [ansi_octave_bands]. The criteria, given as velocities rather than displacements or accelerations because it is argued that the limit to photolithography resolution is image velocity, are reproduced from Reference Gordon1999 in Table 4.1. For the typical feature sizes we would like our microscope to resolve, the VC-B criterion is a fair target. I will use them below to classify the vibration isolation of the confocal microscope.

4.1.2 Microscope isolation concept

What does this mean for our case of a dry DR? The rotary valve motor of the PTR generates pulses with frequency 1.4 Hz. Commercial damping systems that the space constraints in our lab allow to be accommodated, for example the CFM Schiller MAS 25 [CFMSchiller], have resonance frequencies around $f_0=2.5\,\mathrm{Hz}$, implying the first two harmonics of the PTR excitation fall into the amplification regime as discussed above. We are thus right in-between the two regimes and it is a-priori unclear which isolation scheme to choose without detailed mechanics simulations. Hence, the initial isolation concept for the cryostat envisaged mounting the rotary valve motor rigidly to the stiff aluminium item profile frame, which was additionally filled with sand to increase the system's resonance frequency.

However, prompted by a sudden increase in visually observed vibrations in the microscope image, I modified the cryostat frame to house three air springs [CFMSchiller] in the hopes of isolating the microscope from external disturbances. ⁴ To this end, I decoupled the frame from which the cryostat itself is suspended from the support frame standing on the lab ground. Extruding from the square footprint of the support frame at two adjacent corners and the center of the diametrically opposite side, the three air springs are mounted with the base on angle brackets connected to the support frame while their plunger is mounted to a second angle bracket connected to the cryostat frame. The springs are connected by pneumatic tubing to a central pressure regulation panel that is connected to the building's central air pressure line. The vertical placement of the springs is chosen such that when the air springs are deflated the cryostat frame rests on the support frame, establishing the same rigid connection that existed previously. This allows examining the influence of the air springs on the vibration isolation without modifying the setup by simply venting the pressurized air from the springs.

In the following, I will characterize the performance of the system with and without the air springs active using two different methods.

Table 4.1: VCs and International Organization for Standardization (ISO) guidelines

1/3 octave band RM	$1/3$ octave band RMS ($\mu m/s$)		
Workshop (ISO)	800		
Office (ISO)	400		
Residential day (ISO)	200		
Op. theater (ISO)	100		
VC-A	50		
VC-B	25		
VC-C	12.5		
VC-D	6		
VC-E	3		

CFMSchiller

4: As it turned out, the cause was a damaged nanopositioner bearing rather than environmental. Fortuitiously, the endeavour still proved successful and resulted in an improved vibration performance as I show below.

4.2 Accelerometric vibration spectroscopy

The most straightforward method of measuring vibration noise is an accelerometer. These are devices that convert translational forces, for example by means of a loaded spring, into electrical signals. They are mounted rigidly to the device under test (DUT) and typically connected to some sort of signal conditioner providing a constant current bias to the sensor and putting out a voltage proportional to the acceleration. The most sensitive and low-frequency designs use piezoelectric materials like Quartz crystals for sensitivities in the range of 10 V/g with a broadband noise floor of $2 \mu g$ [WilcoxonAccel].

In order to evaluate the vibration level at the sample position, I designed a small angle bracket onto which the accelerometer⁵ can be screwed either in vertical or horizontal direction in the sample puck of the DR, enabling measurements of the displacement noise along the direction of gravity as well as perpendicular to it and the optical axis. The accelerometer is connected to the coaxial cables installed in the cryostat via an adapter cable from imperial 10-32 to SubMiniature version A (SMA) connector. Outside of the cryostat, the signal is routed to a signal conditioner that provides the necessary current bias and outputs a voltage which is digitized by a Keysight 34465A digital multimeter (DMM) connected to the measurement computer. Since the sensor's (conditioned) output is a voltage directly proportional to the acceleration, it is straightforward to compute the displacement power spectral density (PSD) from time series data measured with the DMM using the python_spectrometer package presented in ?? [Hangleiter_pyspeck]. Leveraging the fourier_procfn argument, we can transform the voltage data first to acceleration and then, by integration, to displacement in frequency space as indicated in Listing 4.1.

To assess the impact of the PTR and the suspension, I measured the displacement noise PSD for each combination of the two being switched on and off. The cryostat was closed, its vacuum chamber evacuated, and the magnet, a significant seismic mass, mounted as usual. The measurements are shown in Figure 4.2 together with the band-limited RMS (*cf.* ??),

$$RMS_{S}(f) = \sqrt{\int_{f_{min}}^{f} df' S^{2}(f')}.$$
(4.4)

When the PTR is switched off, the spectra with and without suspension are dominated by broadband vibration noise, although quite some structure around 15 Hz, 33 Hz and 60 Hz can be observed. When it is switched on, the PTR pulses at 1.4 Hz and a large number of its higher harmonics visually dominate the spectra. Clearly, the suspension has a larger impact in this case, matching qualitatively the behavior discussed in Section 4.1. At high frequencies, it manages to almost completely suppress the broadband excitation observed without the suspension. At low frequencies, on the other hand, the PTR harmonics are amplified to the degree that the band-limited RMS is dominated by their contribution. Only at around 10 Hz, the attenuation starts to take effect. Overall, the PTR is found to raise the displacement noise RMS amplitude from 0.5 μm to 10 μm while the suspension, over the entire frequency range, has at best no positive influence.

This result is less than encouraging. At that level of RMS-fluctuations, we'd have a slim chance of resolving micrometer-scale features using the microscope. But is the *absolute* magnitude of displacement noise at

5: Wilcoxon 731–207 kindly lent by Marcus Eßer [WilcoxonAccel].

```
from qutil.signal_processing
    import fourier_space
from qutil.functools import
    chain, scaled
from qutil import const

sensitivity = scaled(1 / 9.9 /
    const.g)
fourier_procfn = chain(
    sensitivity,
    fourier_space.derivative
)
```

Listing 4.1: Functionality to transform the conditioned voltage to displacement in Fourier space.

6: Note the curious peaks slightly offset from the second and third harmonic of the PTR frequency in the spectrum with suspension enabled and PTR disabled. We may speculate that these are due to the PTRs of other cryostats in other labs in the vicinity that are transmitted through the floor. Two were running two rooms over at the time the data was acquired.

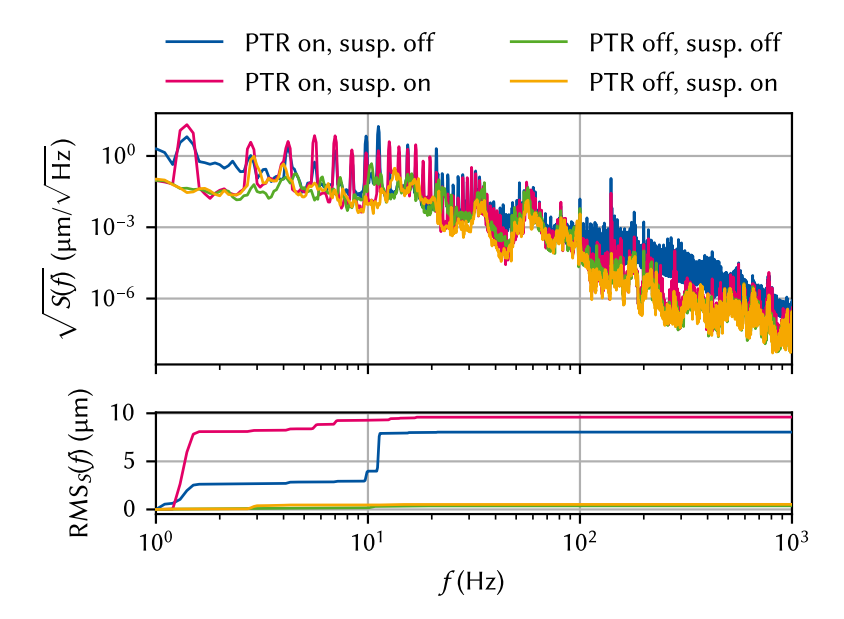


Figure 4.2: Top: displacement noise spectra acquired with the accelerometer at room temperature when the PTR is switched on (blue, magenta) or off (green and orange), and when the air suspension is switched enabled (magenta, orange) or disabled (blue, green). Bottom: band-limited RMS computed from the PSDs in the upper panel (cf. ??). Turning on the PTR increases the RMS noise amplitude by more than an order of magnitude over the entire frequency spectrum. The suspension slightly worsens the total noise because the lowfrequency pulses excite the system close to the air springs' resonance frequency of 2.5 Hz.

the sample position really the correct measure for the microscope performance? Indeed, if the sample oscillates in phase with the objective and ocular lenses as well as the SMF, we will still obtain a perfect imaging fidelity. So actually only the *relative* displacements of sample, lenses, and detection fiber affect the achievable resolution of the microscope. To characterize these, I developed an optical *in-situ* technique to measure the displacement noise based on knife-edge reflectance fluctuations that I will present in the following section.

4.3 Optical vibration spectroscopy

The gate electrodes on our samples are fabricated using two separate lithography processes; first, the smallest structures are written using electron-beam lithography (EBL) in two steps. Then, larger structures on the order of 1 µm and above are written using optical lithography. In the region where the two overlap on the mesa to establish electrical contact, the highly reflective Ti/Au optical gates have a width of 14 µm and a height of 160 nm and lie on top of the poorly reflecting GaAs surface, resulting in a step-like reflectance profile. Scanning perpendicularly across such a straight edge between a poorly and a highly reflecting material is known as a knife-edge measurement and is frequently used to measure the spatial extent of a laser spot [Arnaud1971, Skinner1972, Khosrofian1983]. We can use the same setup to measure the displacement noise; instead of manually shifting our knife edge across the beam spot, though, we measure the reflectance fluctuations induced by the knife edge fluctuating relative to the spot due to external perturbations.

The scenario is sketched in Figure 4.3 in the coordinate system defined by the magnet such that z is along gravity's axis and x is the out-of-plane axis. Focusing the laser (indicated by a dashed circle) onto the edge of the optical gate, we can move the sample using the y-axis nanopositioner and observe a decrease in reflected intensity if the gate is moved away from the laser and an increase if it is moved towards the laser. This gradient

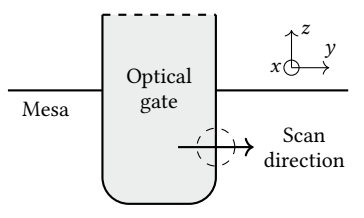


Figure 4.3: Sketch of the region of the sample used for optical vibration spectroscopy. The coordinate system follows the magnet's; z is parallel to gravity, and x is perpendicular to the QW plane. The optical gate extends further north as indicated by the dashed line.

in reflected intensity can be inverted to obtain the vibration noise along y by monitoring the intensity as a function of time.

Let us take a closer look at the reflected intensity when the laser spot has a finite overlap with the edge of the gate. Under the simplifying assumption of a perfectly sharp drop-off and taking the reflectance of the Gold gate to be unity, we can write the reflectance as function of the coordinate perpendicular to the gate edge at y = 0 as

$$R(y) = \begin{cases} 1, & y \le 0 \\ r, & y > 0, \end{cases}$$
 (4.5)

where r is the reflectance of the bare GaAs surface. Assuming a perfect Gaussian (transverse electromagnetic (TEM)₀₀ mode) beam characterized by its waist radius w_0 at which the intensity drops to $1/e^2$ of its maximum value, the laser intensity profile in 1D is given by

$$I(y) = I_0 \exp\left(-\frac{2y^2}{w_0^2}\right),$$
 (4.6)

where $I_0 = P_0/w_0$ with P_0 the total beam power. The power reflected when the spot partially overlaps with the reflectance step can then be expressed as the convolution

$$P_R(y) = R(y) * I(y) = \frac{I_0 w_0}{2} \sqrt{\frac{\pi}{2}} \left[1 - (1 - r) \operatorname{erf}\left(\frac{y\sqrt{2}}{w_0}\right) \right]$$
(4.7)

in the yz focal plane, where erf(y) is the error function.

The function is plotted in Figure 4.4. The contrast that can be achieved is given by 1-r. Furthermore, for $y \in [-w_0/2, w_0/2]$ the function is well-approximated by

$$P_R(y) \approx -I_0(1-r)y + \frac{I_0 w_0}{2} \sqrt{\frac{\pi}{2}}$$
 (4.8)

drawn as a dashed line. Since we measure the photon count rate rather than the power, $\Phi = P\lambda/hc$ with λ the laser wavelength, we rewrite this as

$$\Phi_R(y) = -sy + \frac{\Phi_0}{2} \sqrt{\frac{\pi}{2}}.$$
(4.9)

where we defined the sensitivity

$$s = \frac{\Phi_0}{w_0} (1 - r). \tag{4.10}$$

Hence, to obtain a more sensitive probe for vibrations, meaning that small variations in y lead to large variations in Φ_R , one could either improve the reflectance contrast 1-r, decrease the spot size w_0 , or increase the incident photon flux Φ_0 . In our case, the former two are fixed by the sample and the setup, respectively , whereas the latter is limited by the maximum data transfer rate of the Swabian Instruments Time Tagger 20 counting card, $9 \, \mathrm{MS/s}$.

Starting from Equation 4.9, it is straightforward to obtain the displacement in the vicinity of y = 0 as function of photon flux,

$$y(\Phi_R) = \frac{w_0}{1 - r} \left[\frac{1}{2} \sqrt{\frac{\pi}{2}} - \frac{\Phi_R}{\Phi_0} \right]. \tag{4.11}$$

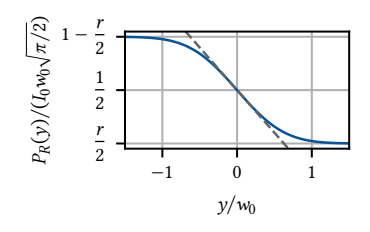


Figure 4.4: Theoretical reflected power for a Gaussian beam of width w_0 and a reflectance contrast of 1-r according to Equation 4.7. The dashed line indicates the leading order approximation at y=0.

7: Note that the smaller w_0 , the smaller also the maximum displacement amplitude that can be resolved as the derivative goes to zero as $y \to \pm \infty$.

To summarize, we can position the laser spot on the edge of an optical gate and record a time trace of the photon flux by using the Time Tagger to count the photons detected by the avalanche photodiodes (APDs) mounted on the side exit of the spectrometer. Using Equation 4.11 we can then convert the flux into a displacement and proceed with the usual spectral noise estimation as explained in Part I.

I will now lay out the experimental procedure of calibrating the system to (implicitly) obtain the parameters w_0 , r, and Φ_0 . The first challenge is obtaining a proper length reference scale. While the nanopositioners on which the sample is mounted do in principle have a resistive position readout, it is extremely unreliable at small displacements. Therefore, I calibrated the relative position using the imaging arm of the optical head. Figure 4.5 depicts the procedure. Illuminating the sample with the white light, I positioned the spot on the edge of the optical gate and imaged the sample with the Thorlabs DCC1545M CMOS camera. I then extracted the position of the edge, in pixels, for several rows to obtain some statistics by fitting a linear function to the edge profile in a small region between two refraction maxima. Repeating this step for different DC voltages applied to the nanopositioner, ⁸ this yields the proportionality factor between the nanopositioner DC voltage, $V_{\rm DC},$ and the position of the gate edge on the camera. By measuring the total width of the gate on the camera image, I obtained the magnification by referencing it to the design width,

$$M = \frac{w[px]}{w[\mu m]} = \frac{116 px}{14 \mu m} \approx 8.3 px/\mu m.$$
 (4.12)

Again performing a linear fit to the data for different voltages then results in the linear transformation from DC voltage to position (upper panel of Figure 4.6). Of course it is also possible to fit the full knife-edge function, Equation 4.7, to the data shown in Figure 4.6. From this, the spot size w_0 and the actual bare GaAs surface reflectivity r can be extracted. Here we are content with the linear approximation; refer to Section B.1 for the full fits.

Lastly, I switched from white light illumination to the laser, focused it onto the edge of a gate, and measured the photon count rate reflected off the sample as a function of $V_{\rm DC}$, from which we can finally extract the desired sensitivity (slope) $s\approx 2.36(2)\,{\rm Mcps/\mu m}$ of count rate over displacement. The data and fit are shown in the bottom panel of Figure 4.6. Clearly, the count rate is linear in the displacement over a large range, indicating that for fluctuations with amplitude on the order of 100 nm RMS, the measurement sensitivity should be sufficiently robust.

We are now at last able to measure the displacement noise using python__| spectrometer. Setting proofn to the linear transformation given in Equation 4.11 and measuring the counts registered by the APDs using the Time Tagger, I obtained the displacement noise PSDs shown in Figure 4.7. A few things stand out. First, rather than the f^{-2} background observed with the accelerometer in Section 4.2, the noise floor is white (S(f) = const.) at approximately 1 nm/ $\sqrt{\text{Hz}}$. To understand why, we need to take a closer look at the counting statistics, which we will postpone for a bit in order to first finish our discussion of the noise spectra. Second, the overall noise level is much – by a factor of 20 RMS – lower than with the accelerometer. We can attribute this to the fact that the optical method is sensitive to relative rather than absolute displacements. If the cryostat and the optical head were infinitely stiff we would measure no displacement noise with this method – intrinsic noise floor notwithstanding –

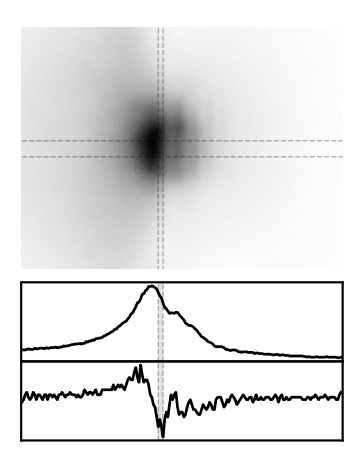


Figure 4.5: Calibration of the length reference scale. The top shows a CMOS camera image (higher intensity darker) of the white light spot on the edge of the optical gate as indicated in Figure 4.3. Several diffraction lines can be seen parallel to the edge. The vertical dashed lines indicate the region in which the intensity slope was fitted. The horizontal dashed lines indicate the extent of rows averaged over. The lower plots show a line cut along the central row of the considered region (top) and its derivative (bottom).

8: The positioners operate in so-called slip-stick mode. In physics terms, the scheme corresponds to alternating adiabatic and diabatic ramps. Slowly ramping up a DC voltage elongates the piezoelectric element by a small amount and moves the positioner table. When quickly jumping back down to 0 V, the table slips and stays in place while the piezo contracts back to its equilibrium elongation. This way, distances much larger than the piezoelectric elongation can be travelled. Staying in the adiabatic regime results in reproducible displacements but also limits the travel.

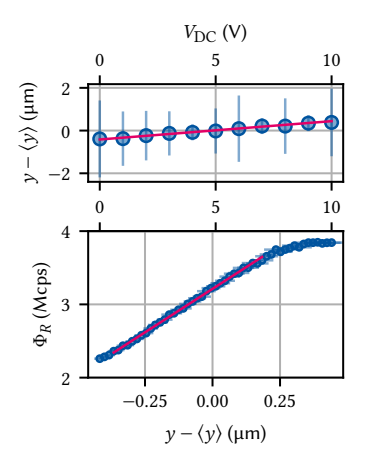
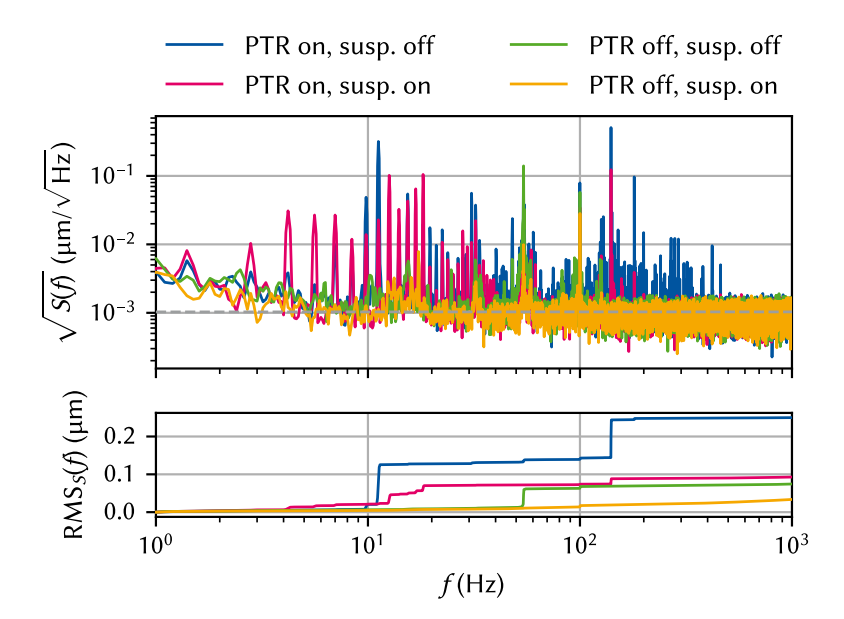


Figure 4.6: Top: linear fit of the edge positions extracted from the analysis in Figure 4.5. Error bars are propagated standard errors of the weighted average of edge positions extracted from different



whereas the accelerometer is still sensitive to oscillations of the cryostat on the air spring fulcrum. In that sense the optical method gives us the more pertinent results because only the displacements seen by the light travelling through the microscope ultimately matter. Third, in contrast to the accelerometer measurements, the RMS amplitude is reduced by half when the suspension is active. Although the harmonics of the PTR frequency of 1.4 Hz are again amplified by the suspension below 10 Hz, raising the band-limited RMS above that with the suspension disabled, there occurs a crossover at the eighth harmonic frequency beyond which the attenuation outweighs the amplification at low frequency. $^{\rm 10}$

4.3.1 Noise floor

The noise floor in the optical vibration measurements shown in Figure 4.7 is qualitatively very different from that observed with the accelerometer. There, the *acceleration* noise floor was white, ¹¹ whereas with the optical method the *displacement* noise floor is white, hinting at a different underlying mechanism.

To elucidate this issue, we model the detection event of a single photon (a "click") arriving at the detector at a random time t_i as a δ -function so that the total flux as function of time is given by

$$\Phi(t) = \sum_{i} \delta(t - t_i). \tag{4.13}$$

Assuming them to be uncorrelated, the time difference between subsequent clicks is exponentially distributed with average rate $\bar{\Phi}$, $|t_{i+1} - t_i| \sim \operatorname{Exp}(\bar{\Phi})$ [**ExponentialDistributionWiki**]. From this it follows that the number of clicks $N(\Delta t)$ within a given time bin $t \in [s, u]$ of length $\Delta t = |u - s|$ is Poisson distributed, $N(\Delta t) \sim \operatorname{Pois}(\bar{N})$, with mean number of counts $\langle N(\Delta t) \rangle = \bar{N} = \bar{\Phi} \Delta t$ [**PoissonDistributionWiki**]. Using the formalism developed in ??, we can now compute the PSD of the stochastic process $\delta N(\Delta t) = N(\Delta t) - \bar{N}$. To this end, observe that because we assumed arrivals to be uncorrelated, $N_{u'}(\Delta t)$ for a time bin starting at t = u' is independent of $N_{s'}(\Delta t)$ for a time bin starting at t = s'. In other words,

Figure 4.7: Top: displacement noise spectra acquired with the optical in-situ method at room temperature when the PTR is switched on (blue, magenta) or off (green and orange), and when the air suspension is switched enabled (magenta, orange) or disabled (blue, green). The dashed gray line indicates the theoretical noise floor derived in Subsection 4.3.1. Bottom: band-limited RMS computed from the PSDs in the upper panel (cf. ??). The PTR has a much smaller effect than when measuring the absolute displacement noise with the accelerometer, increasing the RMS only by a factor of two. While the lowest-order PTR harmonics are amplified by up to an order of magnitude in amplitude with the suspension enabled, they contribute relatively little to the total RMS and are compensated by the superior highfrequency attenuation behavior. The total RMS_S \approx 100 nm with the cryostat in operation is below the typical μm fea-

- 10: It furthermore appears that even a measurement whose sole electronic device is a picosecond-resolution counting card cannot escape 50 Hz power line noise (or in this case its second harmonic).
- 11: Remember that as acceleration is the second time derivative of displacement, in frequency space it is proportional to f^2 times the latter.

the autocorrelation function of $\delta N(\Delta t)$ is nonzero only for the same time bins.

$$C_{\delta N(\Lambda t)}(\tau) = \langle (N_s(\Delta t) - \bar{N})(N_u(\Delta t) - \bar{N}) \rangle = \text{Var}(N(\Delta t))\delta(\tau), \tag{4.14}$$

where $\tau = s' - u'$ and $\delta(\tau)$ is to be understood in a broad sense as zero if $|\tau| > \Delta t$ and $1/2\Delta t$ else. For the Poisson distribution the variance is equal to its mean so that we obtain

$$C_{\delta N(\Lambda t)}(\tau) = \bar{N}\delta(\tau).$$
 (4.15)

In the limit of $\Delta t \to 0$, we can then perform the Fourier transform to obtain the PSD of $\delta N = \lim_{\Delta t \to 0} \delta N(\Delta t)^{12}$

$$S_{\delta N}(\omega) = \bar{N},\tag{4.16}$$

that is, δN is a white noise without frequency dependence. ¹³ $S_{\delta N}$ can be seen as the *instantaneous* number noise PSD.

As a last step, we consider once again discretely sampling the *continuous* process δN with PSD $S_{\delta N}(\omega)$ at rate $f_{\rm s}=\Delta t^{-1}$ in order to find an expression for the PSD of the discrete process $\delta N(\Delta t)$, $S_{\delta N(\Delta t)}(\omega)$. We know from above that ${\rm Var}(\delta N(\Delta t))=\bar{N}$. On the other hand, recall from ?? that also

$$\operatorname{Var}(\delta N(\Delta t)) = \int_{-\infty}^{\infty} \frac{\mathrm{d}\omega}{2\pi} S_{\delta N(\Delta t)}(\omega) = \int_{-f_{c}/2}^{f_{s}/2} \mathrm{d}f S_{\delta N(\Delta t)}(f) \tag{4.17}$$

where the last equation holds true because of the finite bandwidth of the discretely sampled signal. Since $S_{\delta N}$ is white, it follows that $S_{\delta N(\Delta t)}$ is, too, and we can directly evaluate Equation 4.17, obtaining ¹⁴

$$S_{\delta N(\Delta t)}(\omega) = \frac{\bar{N}}{f_{\rm s}}.$$
 (4.18)

To convert to the displacement noise PSD, we can simply convert units using the calibration derived above because if $N \sim \operatorname{Pois}(\bar{N})$ then so $y \sim \operatorname{Pois}(\bar{N}f_{\rm s}/s)$ where s is the slope of the calibration converting displacements to count rates, *i.e.*, the sensitivity (see Figure 4.6 and Equation 4.9). Hence, ¹⁵

$$S_{\delta y(\Delta t)}(\omega) = \frac{\bar{N}}{f_{\rm S}} \times \left(\frac{f_{\rm S}}{s}\right)^2 = \frac{\bar{\Phi}}{s^2}$$
 (4.19)

with $\delta y = y - \langle y \rangle$. This type of noise is known as *shot noise*. It was first studied in the context of electron transport by **Schottky 1918** and results from the discrete nature of, in our case, photons and their stochastic emission times [**Blanter2000**]. For the parameters in the present measurements, $\bar{\Phi} \approx 3$ Mcps and $s \approx 2.36$ Mcps/ μ m (*cf.* Figure 4.6), we obtain a shot noise floor of $S_{\delta y(\Delta t)} \approx 1$ nm/ $\sqrt{\text{Hz}}$ in excellent agreement with the data shown in Figure 4.7 where the theoretical value is indicated by a gray dashed line.

Inserting the theoretical expectation for the sensitivity s, Equation 4.10, into Equation 4.19, we find that

$$S_{\Delta y(\Delta t)}(\omega) = \frac{\epsilon}{\Phi_0} \left(\frac{w_0}{1-r}\right)^2 \tag{4.20}$$

if we identify $\bar{\Phi} = \epsilon \Phi_0$ for some (fixed) setup efficiency ϵ . This shows a

- 12: Despite appearances, $S_{\delta N}$ has units ${\rm cts^2/Hz}$. The discrepancy stems from the difficulty in defining a continuous white noise process.
- 13: Note that we could have also arrived at this result directly by computing the autocorrelation function $\langle \delta N(t) \delta N(t-\tau) \rangle$ from Equation 4.13 with $N(t) = \int \mathrm{d}t \, \Phi(t)$.

14: $S_{\delta N(\Delta t)}$ also has units cts²/Hz.

15: Note that this is the two-sided PSD; to convert to the one-sided version used in this chapter, multiply by two.

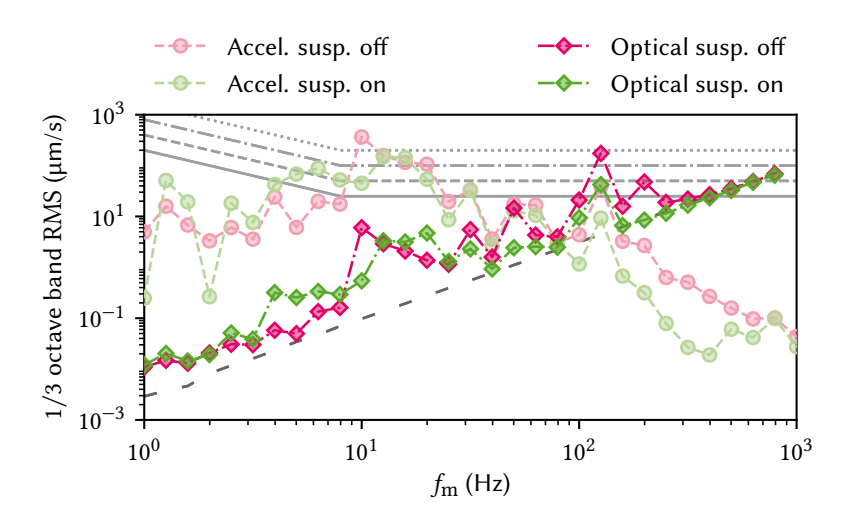


Figure 4.8: 1/3 octave band RMS velocity computed for vibration measurements with the PTR enabled and the suspension disabled (magenta) or enabled (green). Circles (diamonds) show data obtained with the accelerometer (optical method). The VCs VC-B, VC-A and first two ISO levels are indicated as gray lines (solid, dashed, dash-dotted, dotted); see Table 4.1. Accelerometer data are above the VC-B criterion for about three octaves centered around $f_{\rm m} = 10 \, {\rm Hz}$, where even the ISO "residential day" level is breached. Optical data are more favorable, in particular with the suspension enabled (green). Towards high frequencies, the data are dominated by the wideband shot noise floor indicated by the loosely dashed dark gray line, suggesting the true displacement RMS is well below the VC-B criterion.

clear path towards improving the SNR of the method. Just as the sensitivity s is improved by increasing $\bar{\Phi}$ and 1-r and by decreasing w_0 , so is the shot noise floor, albeit quadratically in w_0 and 1-r. For example, for a reduction in spot size by a factor of two from inserting a different objective lens and a tenfold increase in maximum count rate achieved by replacing the counting card with a more powerful model, 16 our simple model predicts a noise floor of $25 \, \mathrm{pm}/\sqrt{\mathrm{Hz}}$, a reduction by a factor of 40.

16: Swabian Instruments offers models with up to 1.2 GS/s, although at that rate the jitter and dead time of the APDs would start to become the limiting factors [SwabianTimeTagger].

To conclude this section, let us come back to the vibration criteria defined in Subsection 4.1.1 and evaluate the microscope based on the two different measurement methods presented in this chapter. The 1/3 octave band RMS velocities computed for the vibration spectra with PTR enabled shown in Figures 4.2 and 4.7 are plotted in Figure 4.8. Based on the data from the accelerometer (circles), the microscope does not meet the targeted level of vibration isolation (VC-B, solid gray line) over three octaves. Because this method of measuring the vibration noise is sensitive to absolute changes, we can understand qualitatively why this is the case if we view the accelerometer at the sample position as the end of a large pendulum whose fulcrum is in the center of the plane spanned by the three air springs. A rough estimate gives a resonant frequency of 0.5 Hz, ¹⁷ implying frequencies in the considered range, [4, 32] Hz, are fairly effective at exciting motion in the pendulum (cf. Subsection 4.1.1). By contrast, with the optical method we do not pick up on such motion because the ocular lens focusing the light into the SMF is fixed in the co-rotating frame with respect to our imagined pendulum. Indeed, the VC velocities computed for this method show that they are orders of magnitude smaller at low frequencies in particular since only deviations from the rigid body picture established above induce a change in signal. Furthermore, the RMS is dominated by the broadband shot noise floor indicated by the loosely dashed dark gray line, implying that the true vibration-induced RMS is well below our targeted VC-B criterion.

17: The center of mass sits close to the magnet approximately $l=1\,\mathrm{m}$ below the springs so that we have $f=(2\pi)^{-1}\sqrt{g/l}\approx 0.5\,\mathrm{Hz}.$

4.4 Routes for improvement

Several improvements could be made to the system if the external conditions would allow it. First, the rotary valve motor should be moved further away from the cold head. As per the initial installation sta-

18: Clearly, this will impact the performance of the PTR to some extent and should therefore be considered carefully.

tus, it is currently connected to the cold head with a flexible hose at a right angle and a distance of roughly 50 cm, which is below the minimum bend radius recommended by Oxford Instruments. Additionally, the term "flexible" is relative here given the pressure of 20 bar. Increasing the length of the hose should reduce its relative rigidity and thereby its ability to transmit vibrations from the motor to the cold head.

Next, the cold head should be mounted firmly to a secondary reference frame, for instance the ceiling or the lower cryostat frame on which the springs rest. An intuitively obvious step, it has also been shown in the literature that decoupling the PTR from the cryostat in this fashion leads to significant improvements in vibration isolation [Olivieri2017]. Acoustic insulation of the room and PTR flex hoses could further improve the low-frequency response of the system [Schmoranzer2019, Oh2021]. Lastly, let me note that there also exist cryocoolers with variable operating frequency that can thus be tuned away from problematic resonances in the system [TransMitPTR].

In Appendix B, I show additional spectroscopy data, including data measured along the gravitational axis in the puck and on the floor of different rooms, which suggests moving to a different laboratory could also benefit the vibration stability, as well as data for different configurations of the PTR motor.

19: Note that the orientation of the motor, which is horizontal with the axis, is also not the recommended configuration.

20: The former option was attempted, but showed no clear improvements in the measurements for reasons unclear, see Appendix B for additional data. It did emphatically deteriorate the interdepartmental atmosphere. Apologies to the institute on the floor above.

appendix plots

Conclusion & outlook



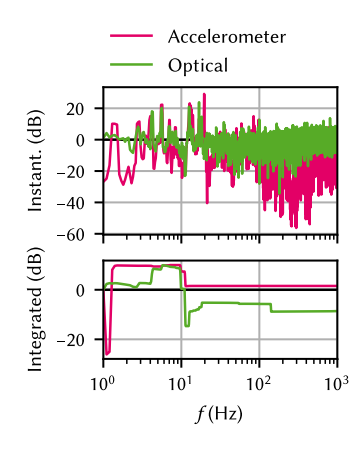


Figure 5.1:

Part III

OPTICAL MEASUREMENTS OF ELECTROSTATIC EXCITON TRAPS IN SEMICONDUCTOR MEMBRANES

Part IV

A FILTER-FUNCTION FORMALISM FOR UNITAL QUANTUM OPERATIONS



Optical coupling



A.1 Collection efficiency

In this section, I derive the expression for the collection efficiency η_c , Equation 3.19 for radiation emitted from a dipole oriented in-plane inside a semiconductor QW with refractive index n and collected with a lens of a given NA. The dipole fields in spherical coordinates (r, θ, φ) in the coordinate system (z, x, y) are given in Equations 3.10 and 3.11. Since we observe the dipole from the side, i.e., perpendicular to its axis, it is useful to rotate the spherical coordinates $(r, \theta, \varphi) \rightarrow (r, \theta, \varphi)$ aligned with the cartesian coordinate system (x, y, z) in Figure 3.3. To this end, observe that with the spherical coordinates

 $x = r\sin\theta\sin\phi\tag{A.1}$

$$y = r\sin\theta\cos\phi \tag{A.2}$$

$$z = r\cos\theta \tag{A.3}$$

we can express the angles in the dipole coordinate system, (ϑ, φ) , in terms of angles of the sample coordinate system, (θ, ϕ) , by

$$\theta = \arctan\left(\sqrt{z^2 + y^2}/x\right)$$

$$= \arctan\left(\csc\phi\sqrt{\sin^2\phi + \cot^2\theta}\right)$$
(A.4)

$$\varphi = \arctan(y/z)$$

$$= \arctan(\sin \phi \tan \theta).$$
(A.5)

The time-averaged Poynting vector, Equation 3.18, is then

$$\langle \mathbf{S}(r,\theta,\phi) \rangle = \frac{1}{2} \operatorname{Re} \left[\mathbf{E}(r,\theta) \times \mathbf{H}^*(r,\theta) \right]$$

$$= \frac{|\mathbf{p}|^2 c k^4}{32\pi^2 \epsilon r^2} \sin^2 \theta \, \hat{\mathbf{e}}_r$$

$$= \frac{|\mathbf{p}|^2 c k^4}{32\pi^2 \epsilon r^2} \left[\cos^2 \theta + \sin^2 \theta \sin^2 \phi \right] \, \hat{\mathbf{e}}_r.$$
(A.6)

Evaluating the integral in Equation 3.17 for the escape cone angle $\theta_{\rm m}=\arcsin({\rm NA}/n)$ thus yields

$$P_{\rm m} = \int_0^{\theta_{\rm m}} \mathrm{d}\theta \sin \theta \int_0^{2\pi} \mathrm{d}\phi \langle S(r, \theta, \phi) \rangle$$

$$= \frac{|\mathbf{p}|^2 c k^4}{32\pi^2 \epsilon r^2} \left[\frac{4\pi}{3} - \frac{\pi}{3n^3} \left(4n^2 - \mathrm{NA}^2 \right) \sqrt{n^2 - \mathrm{NA}^2} \right], \tag{A.7}$$

whereas the total emitted power is the well-known expression

$$\begin{split} P_{\text{tot}} &= \int_{0}^{\pi} \mathrm{d}\theta \sin \theta \int_{0}^{2\pi} \mathrm{d}\phi \langle S(r,\theta,\phi) \rangle \\ &= \frac{|\mathbf{p}|^{2} c k^{4}}{12\pi \epsilon r^{2}}. \end{split} \tag{A.8}$$

fix CS

Together, we therefore find

$$\eta_{\rm c} = \frac{P_{\rm m}}{P_{\rm tot}} = \frac{1}{2} - \frac{1}{8n^3} \left(4n^2 - {\rm NA}^2 \right) \sqrt{n^2 - {\rm NA}^2}$$
(A.9)

as given in the main text.

A.2 Mode profile

In this section, I derive the electric field of a dipole situated inside a dielectric slab and oriented parallel to the surface outside of the dielectric. We use the convention of spherical coordinates from the previous section and consider the electric field given in Equation 3.10 in the rotated coordinate system (r, θ, ϕ) by performing the substitutions given in Equations A.4 and A.5, obtaining

$$\mathbf{E}(r,\theta,\phi) = A(r) \left[E_r(r,\theta,\phi) \hat{\mathbf{e}}_r + E_{\theta}(r,\theta,\phi) \hat{\mathbf{e}}_{\theta} + E_{\phi}(r,\theta,\phi) \hat{\mathbf{e}}_{\phi} \right]$$
(A.10)

with

$$E_r(r,\theta,\phi) = f_r(k,r)\sin\theta\cos\phi \tag{A.11}$$

$$E_{\theta}(r,\theta,\phi) = -f_{\theta}(k,r)\cos\theta\cos\phi \tag{A.12}$$

$$E_{\phi}(r,\theta,\phi) = f_{\theta}(k,r)\sin\phi \tag{A.13}$$

where we defined

$$f_r(k,r) = -\frac{2i}{kr} + \frac{2}{k^2r^2} \tag{A.14}$$

$$f_{\theta}(k,r) = -1 - \frac{i}{kr} + \frac{1}{k^2 r^2}$$
 (A.15)

for conciseness. Now, when the electric field impinges on the surface of the slab, two things must be taken into account: first, it gets refracted, meaning that k is transformed according to Snell's law (Equation 3.16), and second, the transmitted field is modified with the Fresnel transmission coefficients [Hecht2017]

$$t_{s} = \frac{2\sin\theta\sin\theta'}{\sin(\theta + \theta')} = \frac{2n\cos\theta}{n\cos\theta + \nu(\theta)}$$
(A.16)

$$t_p = \frac{t_s}{\cos(\theta - \theta')} = \frac{2n\cos\theta}{\cos\theta + n\nu(\theta)}$$
 (A.17)

where s(p) stands for the component perpendicular (parallel) to the plane of incidence and we defined

$$\nu(\theta) = \sqrt{1 - n^2 \sin^2 \theta}.$$
 (A.18)

In fact, $\hat{\mathbf{e}}_r$ and $\hat{\mathbf{e}}_\theta$ lie in the p plane and $\hat{\mathbf{e}}_\phi$ is parallel to s so that transmission through the interface transforms the electric field components as

$$E_r \to E_r' = t_p E_r = \frac{n^2 f_r(k, r) \left[\sin(\phi + 2\theta) - \sin(\phi - 2\theta) \right]}{2 \left[n\nu(\theta) + \cos \theta \right]} \tag{A.19}$$

$$E_{\theta} \to E_{\theta}' = t_p E_{\theta} = -\frac{2n f_{\theta}(k, r) \nu(\theta) \cos \theta \cos \phi}{n \nu(\theta) + \cos \theta}$$
 (A.20)

$$E_{\theta} \to E_{\theta}' = t_{p} E_{\theta} = -\frac{2n f_{\theta}(k, r) \nu(\theta) \cos \theta \cos \phi}{n \nu(\theta) + \cos \theta}$$

$$E_{\phi} \to E_{\phi}' = t_{s} E_{\phi} = -\frac{2n f_{\theta}(k, r) \cos \theta \sin \phi}{\nu(\theta) + n \cos \theta}.$$
(A.20)

As it should be, the radial component vanishes in the far field, $kr\gg 1$, and only the transverse field components survive. Furthermore, since $\hat{\mathbf{e}}_\phi$ does not depend on θ , only $\hat{\mathbf{e}}_r$ and $\hat{\mathbf{e}}_\theta$ transform according to Snell's law on refraction, resulting in

$$\hat{\mathbf{e}}_r \to \hat{\mathbf{e}}_r' = \begin{pmatrix} v(\theta)\cos\phi \\ v(\theta)\sin\phi \\ -n\sin\theta \end{pmatrix}$$
 (A.22)

$$\hat{\mathbf{e}}_{\theta} \to \hat{\mathbf{e}}_{\theta}' = \begin{pmatrix} n \sin \theta \cos \phi \\ n \sin \theta \sin \phi \\ \nu(\theta) \end{pmatrix} \tag{A.23}$$

in the Cartesian basis defined in Figure 3.3. Finally, we can evaluate the electric field amplitude outside the slab in the Cartesian basis,

$$\mathbf{E}'(r,\theta,\phi) = A(r) \sum_{i \in \{x,y,z\}} E'_i(r,\theta,\phi) \hat{\mathbf{e}}_i, \tag{A.24}$$

with

$$E_x' = f_r(k, r)n\sin^2\theta\cos^2\phi - f_\theta(k, r)\left[\nu(\theta)\cos^2\phi\cos\theta - \sin^2\phi\right]$$
 (A.25)

$$E'_{\nu} = \left[f_r(k, r) n \sin^2 \theta - f_{\theta}(k, r) \{ \nu(\theta) \cos \theta + 1 \} \right] \sin \phi \cos \phi \tag{A.26}$$

$$E'_{z} = \left[f_{r}(k, r)\nu(\theta) + f_{\theta}(k, r)n\cos\theta \right] \sin\theta\cos\phi \tag{A.27}$$

where we dropped the arguments for conciseness.

In principle, the angle Θ and radial distance R for the fields outside the slab would need to be modified when keeping the center of the coordinate system at the dipole source. That is, if we denote the vector from the dipole to the point in the surface where a particular ray exits the slab by r and the vector from that point to the point of observation by r', then $\theta = \arccos(d/r)$ and $\theta' = \arccos([z-d]/r')$, and the spherical coordinate vector $\mathbf{R} = \mathbf{r} + \mathbf{r}'$ with polar angle Θ . Because of refraction, $\theta \neq \theta'$ and hence **R** has norm $R \neq r + r'$. However, outside the slab we are only interested in the far field at the lens where $R, r' \gg d, r$ with d the depth of the dipole inside the slab. Therefore, we can well approximate $\Theta \approx \theta'$ and $R \approx r'$ when dealing with the absolute value of the field, corresponding to placing the center of the coordinate system right below the surface of the slab. For the phase, this approximation likely does not hold well as the radius of the spot on the sample, $\rho_{\mathrm{m}} = d \tan \theta_{\mathrm{m}}$, is on the order of the wavelength $\lambda = \lambda_0/n$ and hence the phase is not constant across the radius ρ , even when observed from the far field. A more rigorous, likely numerical, treatment would be needed to fully account for this.

A.3 Fraunhofer diffraction

The beam focused into the SMF, Equation 3.20, experiences diffraction at the ocular lens aperture. Having approximated the beam as circular, we can write the electric field on the screen, *i.e.*, the fiber end face, as [Hecht2017]

$$\tilde{E}(q) = \frac{|\mathbf{p}|k^2}{2\epsilon} \exp(ikz) \int_0^a \mathrm{d}\rho \, \rho J_0(k\rho q/f_{\rm oc}) E_x(\rho) \tag{A.28}$$

with $E_x(\rho)$ given by Equation 3.22 upon substituting $\theta = \arctan(\rho/f_{\rm ob})$ and $r = \sqrt{\rho^2 + f_{\rm ob}^2}$ and $J_0(x)$ is the Bessel function of order zero. Equa-

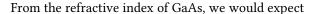
tion A.28 is in general only solvable numerically. Furthermore, note that likely the Fraunhofer approximation is only of limited applicability here since the phase of the wave incident on the lens is not constant across ρ as laid out before.

Vibration spectroscopy



B.1 Knife-edge measurement

In Section 4.3, I used a knife-edge measurement to calibrate the readout of the sample position using the count rate of laser radiation reflected off a lateral reflectance gradient. The gradient was determined by the convolution of the finite spatial extent of the laser spot and a step in reflectance from a Au gate with approximately perfect reflectance and the bare GaAs surface. The same measurement can also be used to extract the reflectance r of the bare GaAs surface as well as the spot size radius w_0 of a Gaussian beam by fitting the theoretical dependence of the reflected count rate on the lateral position, Equation 4.7.



$$r = \left| \frac{n-1}{n+1} \right|^2 \approx 32\% \tag{B.1}$$

at zero temperature [**Talghader1995**]. Figure B.1 shows the same data as Figure 4.6 together with fits to Equation 4.7 in magenta. The dashed line is a fit with r fixed, whereas the solid line is a fit including r as a free parameter. Clearly, the latter matches the data better, resulting in

$$r = 65.1(14)\%$$
 (B.2)

$$w_0 = 0.624(28) \,\mu\text{m}.$$
 (B.3)

The discrepancy in reflectance might be explained by multilayer and thin-film effects given that the sample is only 220 nm thick and warrants closer investigation. In Part III, I perform transfer-matrix method (TMM) simulations to this end. The Gaussian beam waist radius w_0 resulting from the fit is in quite good agreement with the results obtained in Subsection 3.1.3, where we obtained the value 0.60 μ m and 0.84 for the x- and y-direction, respectively (see Table 3.1).

B.2 Additional vibration spectroscopy data

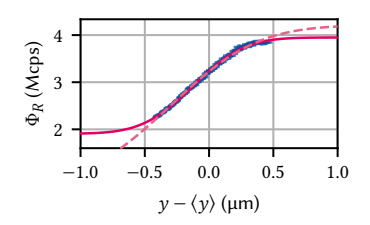


Figure B.1

Special Terms

```
Numbers
2DEG two-dimensional electron gas. 7, 8
APD avalanche photodiode. 26, 29
AR anti-reflection. 5
BBAR broadband anti-reflection. 5
BOB break-out box. 7
BS beam splitter. 5, 10, 16–18
\mathbf{C}
CA clear aperture. 11–16
CCD charge-coupled device. 10
CMOS complementary metal-oxide-semiconductor. 10, 16, 17, 26
cw continuous-wave. 18
DMM digital multimeter. 23
DR dilution refrigerator. 4-6, 10, 20, 22, 23
DUT device under test. 23
EBL electron-beam lithography. 24
GDQD gate-defined quantum dot. 7, 8
HBT Hanbury Brown-Twiss. 18, 26
ISO International Organization for Standardization. 22, 29
LOS line-of-sight. 4
MFD mode field diameter. 11–13
MXC mixing chamber. 4–7
NA numerical aperture. 11-15, 35, 36
NIR near-infrared. 5
OAQD optically active quantum dot. 18
PCC photonic crystal cavity. 14
PL photoluminescence. 18
PSD power spectral density. 23, 24, 26-28
PT1 first pulse tube stage. 5, 20
PT2 second pulse tube stage. 5, 7, 20
```

```
PTR pulse tube refrigerator. 20, 22–24, 27, 29, 30

Q
QD quantum dot. 7–9
QW quantum well. 14, 15, 24, 35

R
RMS root mean square. 20, 22–24, 26, 27, 29

S
SAQD self-assembled quantum dot. 18
SMA SubMiniature version A. 23
SMF single-mode fiber. 10–16, 19, 24, 29, 37
SNR signal-to-noise ratio. 6, 29
SPCM single-photon counting module. 18

T
TEM transverse electromagnetic. 10, 11, 13, 16, 17, 25
TIA transimpedance amplifier. 8
TMM transfer-matrix method. 39

V
VC vibration criterion. 21, 22, 29
```

WD working distance. 12